Lawrence Berkeley National Laboratory
LBL Publications

Title

Synthesis and growth of solution-processed chiral perovskites

Permalink

Journal

ISSN

Authors

Driessen, Sander

Sarigul Ozbek, Sevgi

Sutter-Fella, Carolin

et al.

Publication Date

DOI

Copyright Information

Peer reviewed

TOPICAL REVIEW • OPEN ACCESS

Synthesis and growth of solution-processed chiral perovskites

View the article online for updates and enhancements.

You may also like

Journal of Physics: Energy

TOPICAL REVIEW

Synthesis and growth of solution-processed chiral perovskites

Sander Driessen[1] [iD], Sevgi Sarigul-Ozbek[2] [iD], Carolin M Sutter-Fella[3] [iD] and Shuxia Tao[1,*] [iD]

[1] Materials Simulation and Modelling, Department of Applied Physics, Eindhoven University of Technology, PO Box 513, 5600 MB Eindhoven, The Netherlands
[2] Faculty of Pharmacy, Department of Analytical Chemistry, Acıbadem Mehmet Ali Aydınlar University, Atasehir, Istanbul, 34752, Turkey
[3] Molecular Foundry, Lawrence Berkeley National Laboratory, Berkeley, CA 94720 United States of America
* Author to whom any correspondence should be addressed.

E-mail: s.x.tao@tue.nl

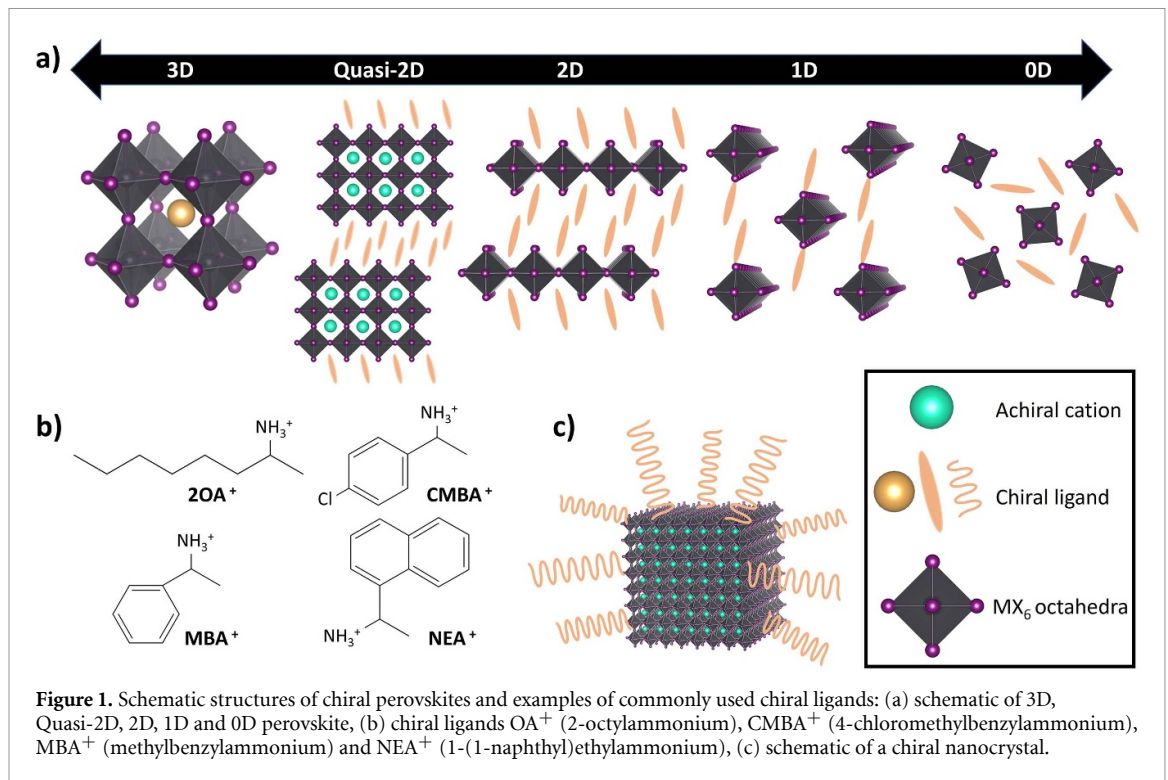## Abstract

In materials science, chiral perovskites stand out due to their exceptional optoelectronic properties and the versatility in their structure and composition, positioning them as crucial in the advances of technologies in spintronics and chiroptical systems. This review underlines the critical role of synthesizing and growing these materials, a process integral to leveraging their complex interplay between structural chirality and distinctive optoelectronic properties, including chiral-induced spin selectivity and chiroptical activity. The paper offers a comprehensive summary and discussion of the methods used in the synthesis and growth of chiral perovskites, delving into extensive growth techniques, fundamental mechanisms, and strategic approaches for the engineering of low-dimensional perovskites, alongside the creation of novel chiral ligands. The necessity of developing new synthetic approaches and maintaining precise control during the growth of chiral perovskites is emphasized, aiming to enhance their structural chirality and boost their efficiency in spin and chiroptical selectivity.

1. Introduction

Over the past decade, three-dimensional (3D) metal halide perovskites have attracted significant research attention. Despite the presence of structural defects, excessive impurities and large compositional variations, this class of materials retains its excellent opto-electronic properties such as long carrier lifetime and high mobility [1, 2]. Another advantage of halide perovskites is their solution processability [3]. 3D perovskites have an empirical formula of AMX_3 and a corner-sharing six-coordinated octahedral crystal structure, where A is a monovalent cation (e.g. $CH_3NH_3^+ = MA^+$, $CH–(NH_2)_2 = FA^+$, or Cs^+), M represents a divalent metal cation (Pb^{2+}, Sn^{2+}), and X is a halide anion (Cl^-, Br^- or I^-). These structures offer great compositional tunability and thus also highly tunable optoelectronic response [4]. For example, instead of cations like MA^+ or FA^+, one can introduce cations with a larger ionic radius by enlarging the carbon chain or adding phenyl-rings. Introducing these larger cations can lead to the formation of low-dimensional perovskites with either metal-halide octahedral sheets, chains or single metal-halide octahedra clusters separated by the organic cations to form 2D, 1D and 0D perovskites, respectively. In these lower dimensional perovskite structures, chiral ligands, containing an asymmetric carbon atom that is terminated with an ammonium tail (NH_3^+), can be introduced. Perovskites of this kind, are commonly referred to as chiral perovskites, and they are schematically shown in figure 1(a). The chiral ligands in these chiral perovskites have been shown to transfer their structural chirality to the inorganic octahedra through asymmetric hydrogen bonding interactions between the H of the chiral ligand (from NH_3^+) and the halide (in the inorganic Pb-X layer), breaking the mirror symmetry of the overall perovskite crystal [5].

Chirality is a term, first coined by Lord Kelvin in 1893 [6], which describes objects that cannot coincide with its own mirror image. Several decades earlier in the 1820s, physicist and astronomer, Sir John Frederick

Figure 1. Schematic structures of chiral perovskites and examples of commonly used chiral ligands: (a) schematic of 3D, Quasi-2D, 2D, 1D and 0D perovskite, (b) chiral ligands OA^+ (2-octylammonium), $CMBA^+$ (4-chloromethylbenzylammonium), MBA^+ (methylbenzylammonium) and NEA^+ (1-(1-naphthyl)ethylammonium), (c) schematic of a chiral nanocrystal.

William Herschel first suggested that chirality in molecules is the cause of optical activity, indicating that the plane-polarized light rotates upon passing through chiral molecules. This phenomena is confirmed by the chemist Louis Pasteur in 1848 by studying the crystallography and optical activity of natural tartaric acid (TA) and paratartaric acid (PTA) obtained via the fermentation of wine [7]. Pasteur, when examining crystals of sodium ammonium paratartrate (SAP), identified that there were two distinct types of TA present that were non-superimposable-mirror-images of each other and he was able to manually separate them. Subsequently, he found that both substances are optically active in solution as observed for TA, with equal rotations in magnitude but opposite in direction. When he mixed these two fractions, however, the rotation of the plane-polarized light disappeared. After this breakthrough discovery, stereochemistry and the chiral molecules attracted great attention. Chiral materials and their mirror images are now known as S- and R-enantiomers whereas a mixture of the two composed of 1:1 ratio is called a racemic compound. These materials have applications in a multitude of fields ranging from medicine, to chemistry, to physics [8].

As described above, the intercalation of chiral organic ligands in halide perovskites made the transfer of chirality from organic molecules into the inorganic metal halide framework, forming chiral perovskite crystals and films. The synthesis of the first chiral perovskites dates back to 2003 by Billing and Lemmerer [9], where a 1D S-methylbenzylammounium lead triiodide (S-MBAPbI$_3$) perovskite was synthesized. Three years later, they also demonstrated the synthesis of 2D R-, S-, and rac-MBA$_2$PbI$_4$ by the slow cooling of a saturated hydroiodic acid solution in which a lead oxide- and MBA-powder are dissolved stoichiometrically [10]. However, a study of the chiroptical activity, like Pasteur performed for PTA, was not carried out up and until 2017 by Ahn *et al* [11], which sparked wide interest in these materials in the field of chiral photonics. The experimentally reported chiral perovskites are typically low-dimensional, because the ionic radius of the chiral ligands are too big to fit in the Pb-based 3D perovskite framework and form a stable structure. To obtain 3D chiral perovskites, one needs small organic alkylammonium cations. Although predicted to be thermodynamically stable by Long *et al* in 2019 [12], it took until recently for 3D chiral perovskites to be synthesized using Rb to form a larger inorganic framework such that a chiral cation could be incorporated [13]. Hence, chiral perovskites are commonly low-dimensional structures intercalated with chiral ligands, of which some extensively studied examples such as MBA (methylbenzylammonium) and NEA (1-(1-naphthyl)ethylammonium) are shown in figure 1(b). Chirality can also be introduced in perovskite nanocrystals by crafting chiral ligands on the surface, which distort the surface of the nanocrystal. A schematic view of a chiral nanocrystal is shown in figure 1(c) where an achiral nanocrystal is passivated solely with chiral ligands.

The combination of chirality and the remarkable opto-electronic properties of perovskites make chiral perovskites a promising class of materials for the study of emergent optoelectronic properties and the

exploration of novel devices and applications. Firstly, these materials exhibit the chiral-induced spin selectivity (CISS) effect, offering novel applications in spintronics like spin-photovoltaic devices, spin-valve devices and spin-LEDs [14–16]. Secondly, these materials also show chiral optical activity (COA), i.e. differentiated absorption or emission of circular polarized light, providing a means for chiroptical application such as a novel way for circularly polarized light (CPL) detection [17]. A third characteristic of this class of materials is that they exhibit non-linear optical properties [18]. These properties make them promising candidates for applications such as lasers and ultrafast laser modulators.

While the fundamental mechanisms of CISS and COA are not yet fully understood, it is commonly accepted that both effects are strongly correlated with the structural chirality of the chiral perovskites. Although the full structure-property relation has yet to be established, a recent work has identified a whole set of structural descriptors and the mechanisms of structural chirality transfer [19, 20]. The large compositional space in both chiral organic ligands as well as the inorganic metal halide framework offer therefore large tunability in their physicochemical properties. This is essential for not only the fundamental understanding of CISS and COA, but also the optimization of the function of the materials and finally the operation of novel devices. Many existing literatures on chiral perovskites indeed primarily focus on the characterization of the chirality of the structures, COA and CISS effects, with the aim of understanding their complex correlations. For overview on these topics, we refer to earlier reviews by Ahn *et al* focusing on COA [21] and by Lu *et al* [22], which focuses more on the CISS effect. For a review on non-linear optical properties, we refer to the work by Xu *et al* [23]. For an overview of the general optoelectronic properties of chiral perovskites, see the reviews by Long *et al* and Dong *et al* [24, 25].

In this review, we focus on an important, yet less discussed aspect: the synthesis and growth of chiral perovskites. Given the high importance of structural chirality, synthesizing a smooth and defect-free material is crucial. The correlation between preparation methods and the CISS effect remains unclear. However, our goal is not to elucidate this correlation, but to objectively describe the literature on the preparation of perovskites exhibiting chiroptical properties. Due to limited number of publications focusing on reporting the synthetic chemistry and growth mechanism of chiral perovskites, we first focus on the general growth methods, mechanisms, and engineering strategies of low dimensional perovskites (section 2), and then the synthesis methods of commonly used chiral ligands (section 3). These two sections are followed by analysis of available literature focusing on the growth mechanisms of chiral perovskites in section 4, highlighting strategies for optimizing their unique optoelectronic properties that is connected with their chemical compositions and structural chirality. Finally, a discussion is provided to stimulate novel synthetic and growth methods for the optimization of existing, and the discovery of new functionalities of this fascinating class of materials.

2. Growth methods, mechanisms and engineering strategies of low dimensional perovskites

Motivated by the fact that a majority of synthesized chiral perovskites are low dimensional, this section summarizes growth methods, as well as crystallization and nucleation mechanisms of general low dimensional perovskites. A few very important aspects, including compositional (changing A, M or X) and dimensionality (comparing 2D vs 1D vs 0D) engineering, and as well as solvent and additive engineering are analyzed. Along the analysis, strategies to obtain low-dimensional perovskites with narrow *n*-phases distribution, controlled growth orientation and smooth film morphology, are discussed.

2.1. Growth methods and mechanisms
Low-dimensional 2D layered perovskites offer great materials design flexibility by relaxing the size requirements for the A-site cation. 2D structures consist of alternating layers of inorganic metal halide octahedra and large organic site cations (figure 1(a)) referred to here as A'. The inorganic corner sharing BX_4-octahedral layer can be separated by monolayers of divalent cations (referred to as Dion-Jacobson, DJ) or bilayers of monovalent cations (referred to as Ruddlesden-Popper, RP) leading to $A'BX_4$ and A'_2BX_4 stoichiometries, respectively. One can also synthesize 2D perovskites that have inorganic layers with a thickness of more than one octahedra ($n > 1$) which are commonly referred to as Quasi-2D perovskites. RP phases with monovalent A' adapt a general formula $A'_2A_{n-1}B_nX_{3n+1}$ and are the most widely studied. Here, n refers to the number of inorganic octahedral layers of which examples are shown in figure 2(a).

In general, solution-processed thin films of low-dimensional perovskites can be synthesized in two ways. Firstly, the lead source (PbX_2) can be dissolved together with the organic ammonium-halide salt in a polar aprotic solvent. A second method is to prepare a stoichiometric perovskite single crystal powder which is subsequently dissolved in a solvent of choice to fabricate a thin film.
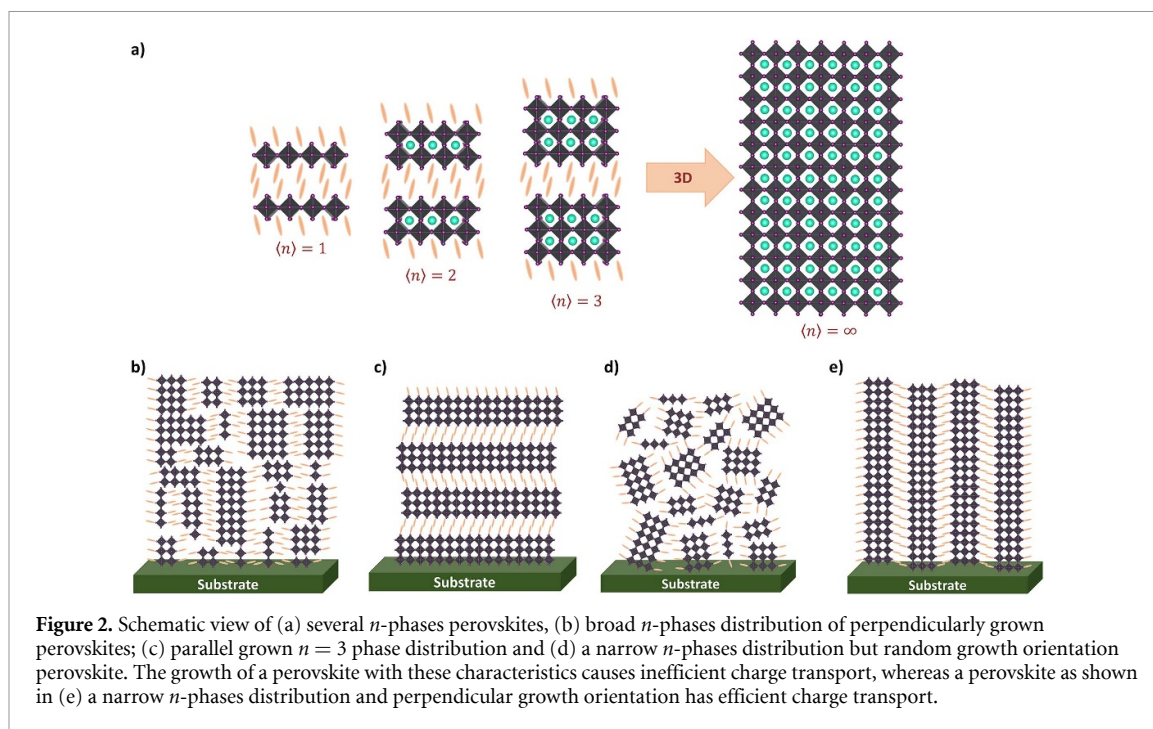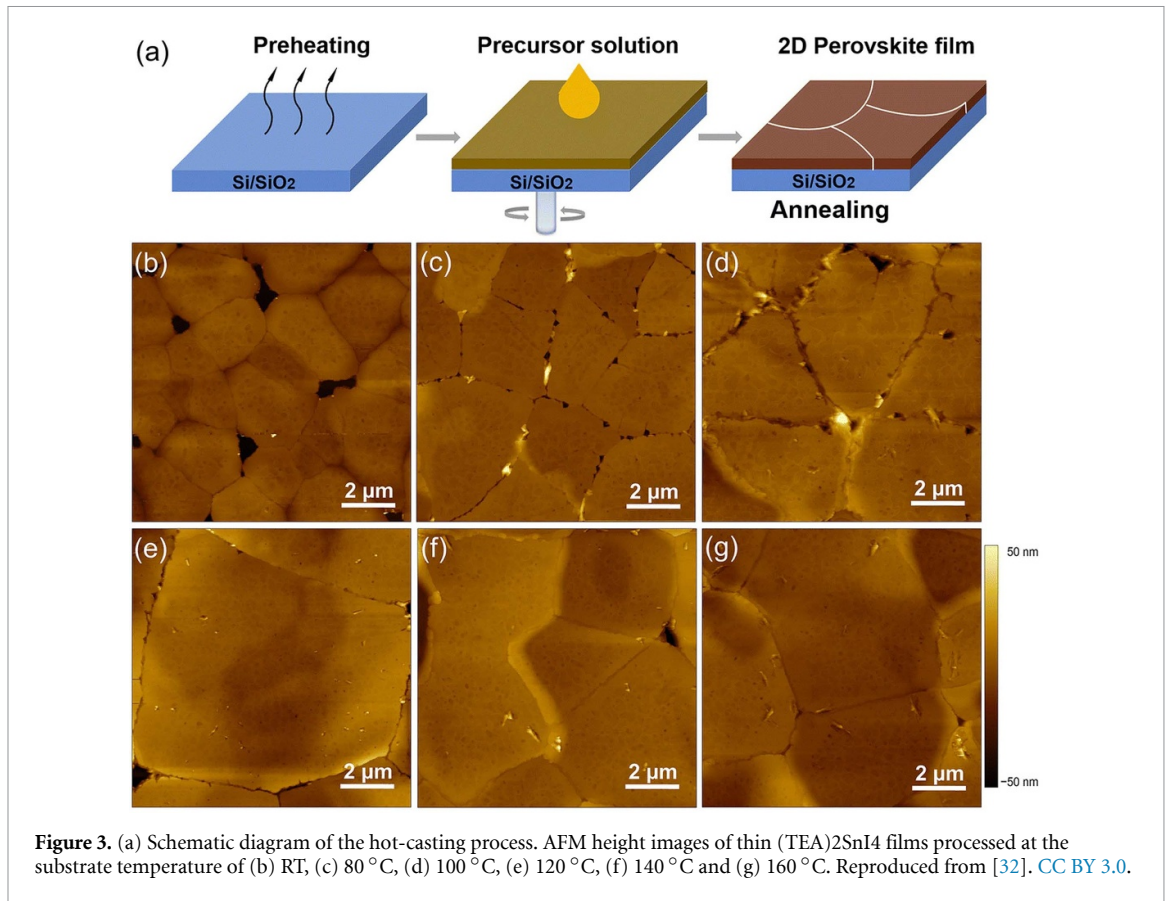
Figure 2. Schematic view of (a) several *n*-phases perovskites, (b) broad *n*-phases distribution of perpendicularly grown perovskites; (c) parallel grown *n* = 3 phase distribution and (d) a narrow *n*-phases distribution but random growth orientation perovskite. The growth of a perovskite with these characteristics causes inefficient charge transport, whereas a perovskite as shown in (e) a narrow *n*-phases distribution and perpendicular growth orientation has efficient charge transport.

Such single crystals can be synthesized in a variety of ways. One may, for example, use the temperature-lowering or a solvent-evaporation crystallization technique, where the solubility of the perovskite precursors decreases upon lowering temperature [26] and the degree of supersaturation increases upon solvent evaporation [27], respectively, both leading to crystal formation. One may also employ an antisolvent-assisted strategy where an antisolvent is gradually diffused into the solution containing the crystal precursors, which promotes the precipitation of single crystals [28]. A more environmentally friendly method is aqueous pH-controlled synthesis, as no toxic solvents are used, but it is difficult to apply to perovskites with $n > 1$ [29]. In this method, the crystals are prepared in deionized water, and the reaction conditions, such as the pH and temperature, need to be carefully controlled. Wang *et al* showed the synthesis of chiral (*R/S*)-α-(PEA)$_2$PbI$_4$ single crystals where hydriodic acid was used to dissolve the PbI$_2$ in the deionized water [30]. After this salt was dissolved, an aqueous solution of MA$^+$ and the organic spacer cation may then be added after which the solution crystallizes into the desired crystal. It is crucial for the solution to have a pH under 4, as otherwise a precipitate of Pb(OH)$_2$ was formed. The synthesis is performed at room temperature, thus MAPbI$_3$ was not allowed to form, and the MA$^+$ cation remained at the surface, helping to maintain the ion balance.

The most basic fabrication of 2D or quasi-2D halide perovskite thin films is by one-step spin coating. This approach consists of depositing the precursor solution on a spinning substrate for solvent removal after which the film is annealed. This approach is used often because of its straightforwardness, but it typically yields poor surface morphology and a wide range of *n*-phases in the film [31]. Most spin-coating processes take place at room-temperature, but one can also preheat the substrate as schematically shown in figure 3(a). This approach is frequently referred to as hot-casting. The effect of the substrate temperature on a (TEA)$_2$SnI$_4$ perovskite is investigated by Wang *et al* [32]. One can see an AFM image of the (TEA)$_2$SnI$_4$ perovskite thin film spin-coated at room temperature in figure 3(b). A lot of small grains can be observed in this film. In contrast, the spin coated thin films on a substrate at higher temperatures show a substantially increased grain size as shown by AFM images in figures 3(c)–(g). Next to a large grain size, also a more vertical growth orientation of films with respect to the substrate has been observed when hot-casting was applied [33, 34]. The advantage of vertical orientation is a more efficient charge carrier extraction from the film. However, a too high substrate temperature should be avoided as this can cause too fast solvent evaporation which can lead to degradation of the film quality and even incomplete surface coverage on the substrate when the temperature changes rapidly [35].

Next to the hot-casting method, a thermal procedure that can be performed in the synthesis of perovskites is a pre-crystallization annealing step. In this procedure, the substrate is heated on a hotplate with minimal spin-induced convection after which a spin-coating step is employed. This has proven to have a positive effect on the vertical growth orientation just like hot-casting [36]. Another way to make 2D or quasi-2D halide perovskites is via dissolving pre-synthesized single crystals instead of a stoichiometric
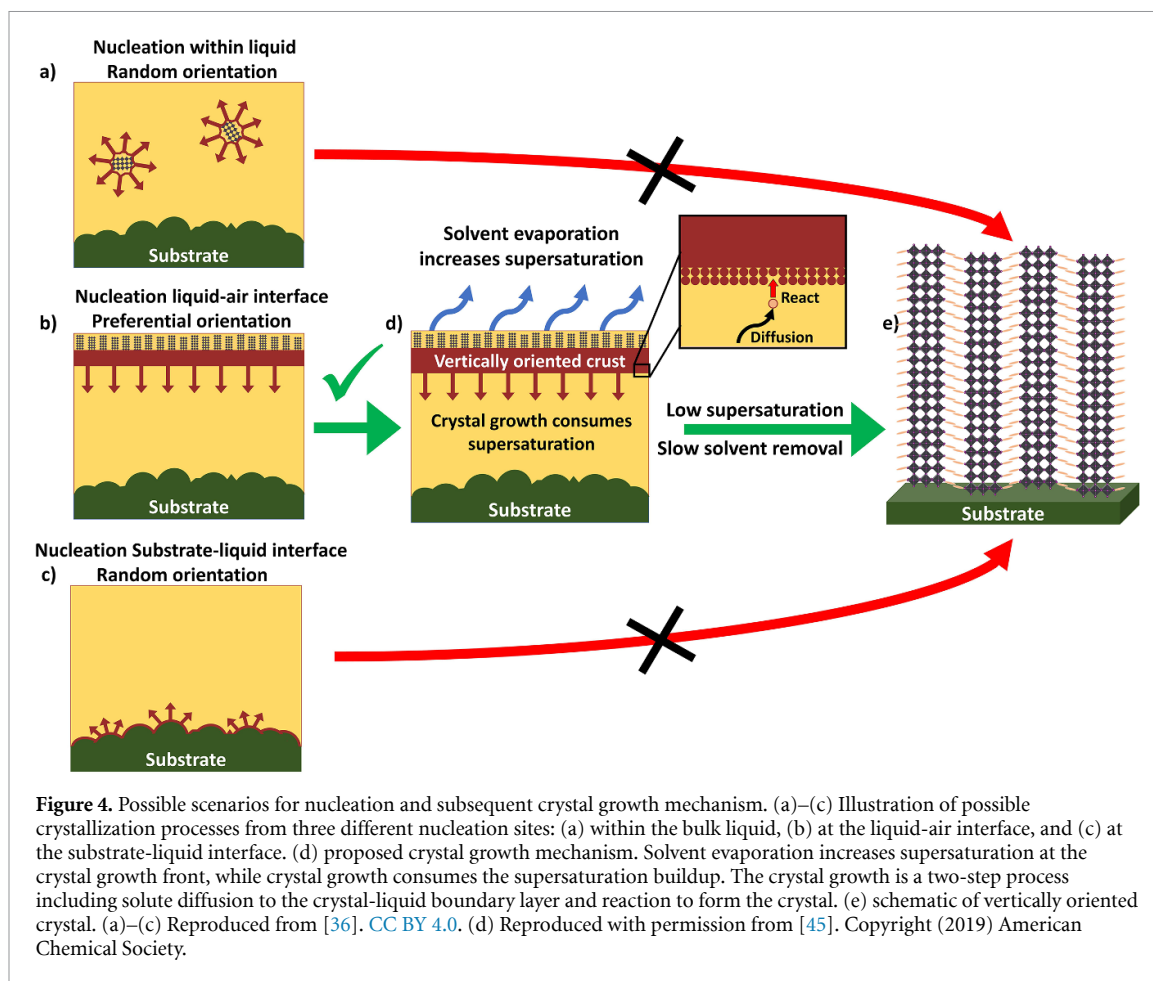
Figure 3. (a) Schematic diagram of the hot-casting process. AFM height images of thin (TEA)2SnI4 films processed at the substrate temperature of (b) RT, (c) 80 °C, (d) 100 °C, (e) 120 °C, (f) 140 °C and (g) 160 °C. Reproduced from [32]. CC BY 3.0.

mixture of precursors. For example, Sidhik *et al*, investigated how to exploit this to improve phase purity in a $BA_2MA_2Pb_3I_{10}$ perovskite [37]. In this investigation, millimeter-sized crystals were dissolved and a seed-assisted nucleation and growth-process was revealed. These seeds (∼200 nm) preserve the memory of the dissolved single crystals and a superior phase purity is reached compared to the classical spin-coating method, but a phase-pure film is not obtained using this method. As shown by Stoumpos *et al* [38], to obtain a high yield of phase pure $(BA)_2(MA)_{n-1}Pb_nI_{3n+1}$ single crystals, it is necessary to use a deficiency of BA in the starting solution.

Recently, the chiroptical signals from single crystals and thin films were compared in $(R/S\text{-NEA})_2PbBr_4$ by Li *et al* and the chiroptical signal from the single crystal was determined to be 1-2 orders of magnitude larger than the one for thin films [39]. It is hypothesized that the lower CD signal has two causes that relax the selection rules, thereby reducing the CD signal of the films. One cause is that the chiral spacers disrupt crystallization, yielding non-crystalline, amorphous domains. Next to this, the introduction of a high density of grain boundaries with randomly oriented grains and defects disrupts the long range order. Hence, the thin film formation needs to be well understood and improved, to obtain thin films with a comparable chiroptical response to single crystals.

Regardless of the thin film preparation method from chemical solutions, the thin-film coating step to obtain the perovskite film always involve the interactions of perovskite species with solvents. Such interactions can generally be split into three stages.

Firstly, before nucleation of perovskites occurs, the solvent evaporates until the concentration of the solution increases up to the solubility limit. When the solvent evaporates more, a stage of supersaturation is reached but no nucleation occurs yet until the system overcomes the nucleation barrier. In this stage the system consists of unoriented colloidal sol-gels, where only 1D solvent-coordinated non-perovskite precursor phases exist [40].

Secondly, when the nucleation barrier is overcome, nucleation occurs where the precursors form perovskite phases. In general nucleation can happen at three distinct places in the solution, which are within the liquid film, from the liquid-substrate interface and from the air-liquid interface. This is schematically shown in figures 4(a)–(c). The nucleation sites have important consequences for the growth orientation. Nucleation occurring within the liquid film would yield a random orientation due to the isotropic environment [41]. An uneven substrate surface would cause a random growth orientation as well. Nucleation from the liquid-air interface could facilitate perpendicular growth orientation to the substrate

Figure 4. Possible scenarios for nucleation and subsequent crystal growth mechanism. (a)–(c) Illustration of possible crystallization processes from three different nucleation sites: (a) within the bulk liquid, (b) at the liquid-air interface, and (c) at the substrate-liquid interface. (d) proposed crystal growth mechanism. Solvent evaporation increases supersaturation at the crystal growth front, while crystal growth consumes the supersaturation buildup. The crystal growth is a two-step process including solute diffusion to the crystal-liquid boundary layer and reaction to form the crystal. (e) schematic of vertically oriented crystal. (a)–(c) Reproduced from [36]. CC BY 4.0. (d) Reproduced with permission from [45]. Copyright (2019) American Chemical Society.

independent of what substrate is used [42, 43]. It has been shown by Bakr *et al* that the surface tension plays a significant role in the nucleation at the liquid-air interface [44], leading to the higher nucleation barrier in the bulk of the solution than at the liquid-air interface. However, the fundamental mechanism behind the growth orientation of 2D perovskites is not fully understood and further investigation will be helpful to gain more insights of the underlying mechanisms.

The final stage of solvent evaporation is the growth of the perovskite phase. During this stage the solute diffuses to the nucleated perovskite site and subsequently is consumed by a reaction of the solute at the crystal-liquid interface. This process is schematically shown in figure 4(d). The consumption of solute decreases supersaturation and the nucleation rate is suppressed. To produce vertically oriented perovskites, a continuous crystal growth without additional nucleation events is necessary. Therefore, a low supersaturation condition, and thus a slow solvent removal rate, is crucial to produce vertically oriented perovskites [45]. Apart from a preferential growth orientation, slow growth of the crystals should also yield larger grain size and an increased purity. As will be discussed, below the rate of growth can be tuned by compositional engineering of solvents, additives, and applying thermal treatments.

The precise control in the growth stage is in particular important for growing pure n-phases quasi-2D perovskites ($n > 1$). The growth of the quasi-2D perovskites commonly yields a distribution with 2D perovskites ($n = 1$) and low n-phases ($n = 2$) quasi-2D perovskites close to the substrate, to higher n-phases ($n = 3, 4, 5$) in the middle and finally to 3D perovskites ($n = \infty$) at the top of the solution [40, 46]. This can be explained by the distribution of the bulky A' cations and their diffusion properties.

First of all, due to the presence of the substrate, a gradient in the bulky A'-cation concentration is observed. Because the surface energy at the substrate is typically lower than the surface energy at the liquid-air interface, bulky cations with low surface energy, like PEA, will tend to be more concentrated at the substrate than at the liquid-air interface [47].

Secondly, the larger cation A' typically diffuses slower than the smaller cation A towards the reaction site [48]. Due to the faster diffusion of the A-cation to the site, at the start higher n-phases will be formed and only later the A' cations will be consumed and lower n-phases will be present. To suppress this type of phase

distribution, several strategies can be used. These include improving the homogeneity of the distribution of large organic cations [49], increasing their diffusion rates, or slow down the overall growth of the systems.

Finally, up and until now the composition of n-phases and their growth orientation have been treated separately in this work. However, they are dependent on each other. Quasi-2D perovskite crystals with low n-phases ($n < 3$) tend to grow parallel to the substrate whereas higher n-phases perovskites generally grow perpendicular to the substrate. It has been proposed that this effect has to do with the interaction of the substrate with the perovskite due to van der Waals and electrostatic interactions but a systematic investigation is lacking [50, 51].

Next to considering the crystallization kinetics, one can also view the process from a thermodynamic perspective. The important variable here is the Gibbs free energy $\Delta G = \Delta H - T\Delta S$, where ΔH is the enthalpy of formation, T is the temperature and ΔS is the change in entropy. For ordered perovskite, the $(-T\Delta S)$ term is strictly positive and thus a negative enthalpy of formation is desirable. Hence to know what n-phases are preferentially formed, the enthalpy of formation needs to be determined for a range of n-phases. This is done by Soe *et al* for a Ruddlesden-Popper perovskite $(BA)_2(MA)_{n-1}Pb_nI_{3n+1}$ for n-phases ranging from $n = 1$ to $n = 7$ using isothermal solution calorimetry [52]. It is suggested that low n-phases are thermodynamically more favorable, due to their more negative enthalpy of formation, compared to high n-phases. Therefore, when preparing the precursor for a high n-phases perovskite, it will likely yield a mixture of lower n-phases perovskites. However, when a pure 2D perovskite is targeted with $n = 1$, no small cations are present and thus physically no phase impurities can be formed. Therefore, the formation of such perovskites should yield a narrow n-phases distribution.

2.2. Compositional and dimensionality engineering

The precursor composition plays an important role in the growth. For example, in the growth of a $(iso\text{-}BA_2MA_4(Pb_xSn_{1-x})_5I_{16}$ perovskite, the ratio of metal cations (tin to lead) in the perovskite is shown to be important in the growth process because Sn has stronger covalent bonding with I than Pb [53]. This stronger bonding causes smaller nucleation centers and faster growth. Also due to the smaller size of Sn compared to Pb, bulky organic ligands fit more poorly in SnI_x complexes. Thus, Sn rich precursors tend to form nano-sized disordered phases without any long-range vertical growth. The ideal ratio found for the $(iso\text{-}BA_2MA_4(Pb_xSn_{1-x})_5I_{16}$ perovskite is for $x = 0.7$.

Besides metal cations, the A cations and their interaction with solvent, often characterized by their solubility, plays also a significant role. A notable example is $(X\text{-}PEA)_2MA_3Pb_4I_{13}$ (X = F, I, Cl, Br), where the solubility decreases for different spacer cations with the trend PEAI > F-PEAI > Cl-PEAI > Br-PEAI [54]. For the perovskites with Cl-PEA and Br-PEA as spacer, due to their low solubility, small n-phases nucleate at an early stage, leading to a random n-phases distribution. Conversely, for the perovskites with PEA and F-PEA as spacer the perovskites with large n-phases nucleate first, leading to the above discussed distribution of low n-phases at the substrate to high n-phases at the top side. Also, it is found here that the perovskite containing PEA spacer functionalized with F, exhibits improved crystallinity and a growth orientation perpendicular to the substrate with respect to the non-functionalized PEA spacer.

Above, the formation of 2D and quasi-2D perovskites have been discussed. However, sometimes when a mix of precursors is prepared to obtain such a structure, a lower dimensional perovskite is formed. For example, when attempting to form a low n-phases structure of a 2D RP MA-based lead-iodide perovskite containing propylammonium (PA) as bulky spacer, a 1D perovskite is obtained [55]. Such 1D perovskite consists of chains made of corner-sharing, edge-sharing and face-sharing metal halide octahedra with bulky organic spacers separating them. These different connectivity types are shown in figure 5(a). Often, these perovskites can consist of a mixture of these connectivity types, including linear (i.e. $C_4N_2H_{14}PbBr_4$ [56]), bilinear (i.e. $((C_6H_{16}N_2)_3)Pb_2Br_{10}$ [57]), step-like (i.e. $C_6H_{18}N_2)BiI_5$ [58]), and tubular (i.e. $(C_6H_{13}N_4)_3Pb_2Br_7$ [59]), and their chemical formulas depend on their type of connection and the type of bulky organic cation [60, 61]. These types of 1D perovskites are shown in figure 5(b). It is unclear under which conditions which type of chain or connection type is established.

Apart from the effect of the organic spacer, the molar ratio of the organic spacer and the metal cation is also important to control the dimension of the perovskite. This has been shown in the case of the lead-iodide based perovskite with NEA as an organic spacer [62]. When a ratio of twice as much NEA^+ as Pb^{2+} is in the precursor, a 1D perovskite is formed with formula $(R\text{-}, S\text{-}NEA)PbI_3$, whereas if a ratio 1:2 of NEA^+ versus Pb^{2+} is present, a 2D perovskite is formed with the formula $(R\text{-}, S\text{-}NEA)_2PbI_4$.

2.3. Solvent engineering

There are several solvents that can be used for the synthesis of low-dimensional perovskites. Hydrohalic acids (HX, X = Cl^-, Br^- or I^-) can be used as solvents and can also function as a halide source [63, 64]. The type of halide must match the halide in the desired perovskite. Because a large excess of this HX type halide is
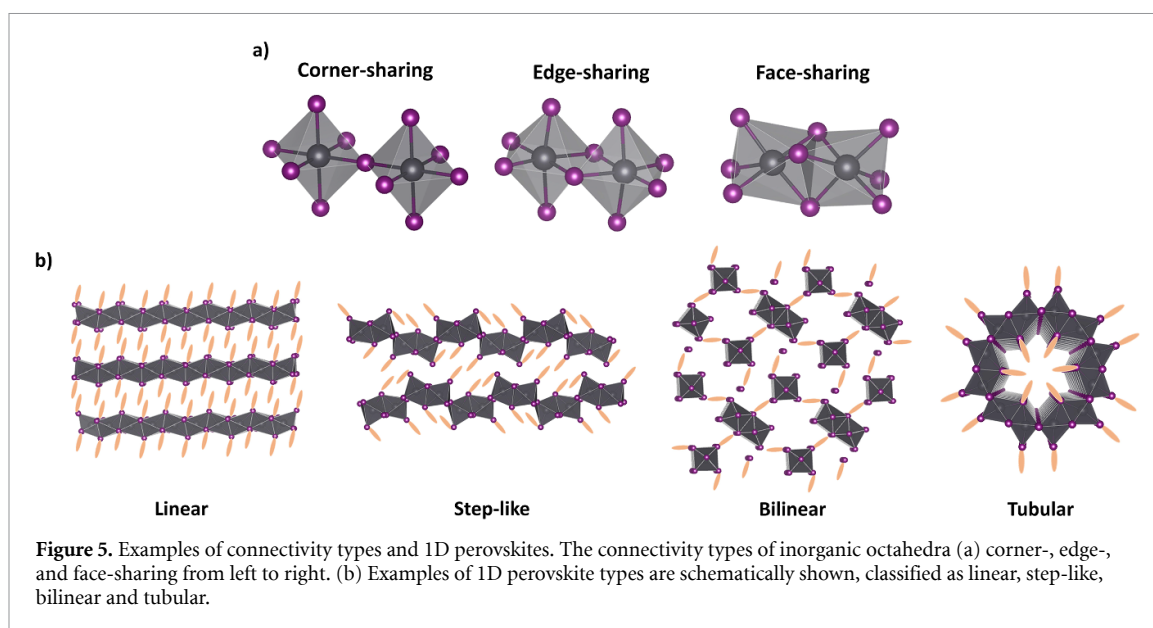
Figure 5. Examples of connectivity types and 1D perovskites. The connectivity types of inorganic octahedra (a) corner-, edge-, and face-sharing from left to right. (b) Examples of 1D perovskite types are schematically shown, classified as linear, step-like, bilinear and tubular.

present in the solution, the resulting perovskite will have this type of halide irrespective of the metal or organic cation salts. The interplay of the solvent with the organic cations in the solution is very important, which is often characterized by their solubility. In general, a precursor containing a greater organic component (e.g. lower *n*-phases) is less soluble in HX than a precursor containing a smaller organic component. To obtain the desired stoichiometric ratio, for a compound with greater organic component and is thus less soluble in HX, the molar ratio needs to be changed to contain a less than stoichiometric ratio of the organic spacer. Conversely, for a compound that is more soluble in HX, the precursor needs to contain either the stoichiometric ratio or more [65]. Hence for every spacer cation, this needs to be optimized per *n*-phase for their solubility. Also there are for example spacers that are too insoluble in HX such as 1-(2-naphthyl)methanammonium (NMA) in $(NMA)_2Pb(X = Br, Cl)_4$ [66], and other cations with bigger organic components which for example contain pyrene and pyrelene groups [67].

In these cases other solvents, such as, strong polar aprotic organic solvents, including dimethyl sulfoxide (DMSO), γ-butyrolactone (GBL), N,N-dimethylformamide (DMF) and dimethylpropyleneurea (DMPU) may be used. The structures of these solvents are shown in figure 6(a). Commonly used solvents in low-dimensional perovskites are DMF and DMSO. These solvents have varying properties like polarity, viscosity, boiling point, surface wettability, and coordination ability which will cause large differences in the evaporation rate of solvents and the formation of intermediates, which directly affects the crystallization kinetics of 2D perovskites [68, 69]. The most important property to consider is the coordination ability of the solvent with the metal halide complexes in the solution, which is best described by the Gutmann Donor number D_N and for several solvents this number is plotted in figure 6(b) [70, 71]. This coordination ability of the solvent is directly correlated to the intermediate phase formation in the solution. These intermediate phases facilitate the nucleation site with precursor material when the solvent releases them. A stronger coordination ability with the metal halide complexes can form more stable intermediates, therefore it can slow down crystallization and thus improve the morphology, growth orientation and the *n*-phases distribution [72].

For Pb-based low-dimensional perovskites, typically a mixture of DMSO and DMF is used to control the crystallization kinetics. The DMSO here slows down the growth (higher D_N) and DMF speeds it up (lower D_N). The molar ratio of DMSO and DMF here needs to be optimized for every bulky cation to yield a perovskite with preferential orientation and good morphology [73, 74].

However, for Sn-based perovskites, a more parallel growth orientation has been observed when DMSO is used whereas when DMF is used a more vertical orientation is observed [75]. A problem encountered with the Sn-based perovskites is the oxidation of Sn^{2+}. It has been shown that DMSO oxidizes the Sn^{2+} in the precursor solution [76]. This oxidation effect causes the undesired formation of dimethylsulfide and SnO_2 in the crystals. To eliminate these impurities, one can use a highly coordinating solvent such as DMPU, which also suppresses oxidation as shown by Heo *et al* in the formation of $(PEA)_2SnI_4$ [77].
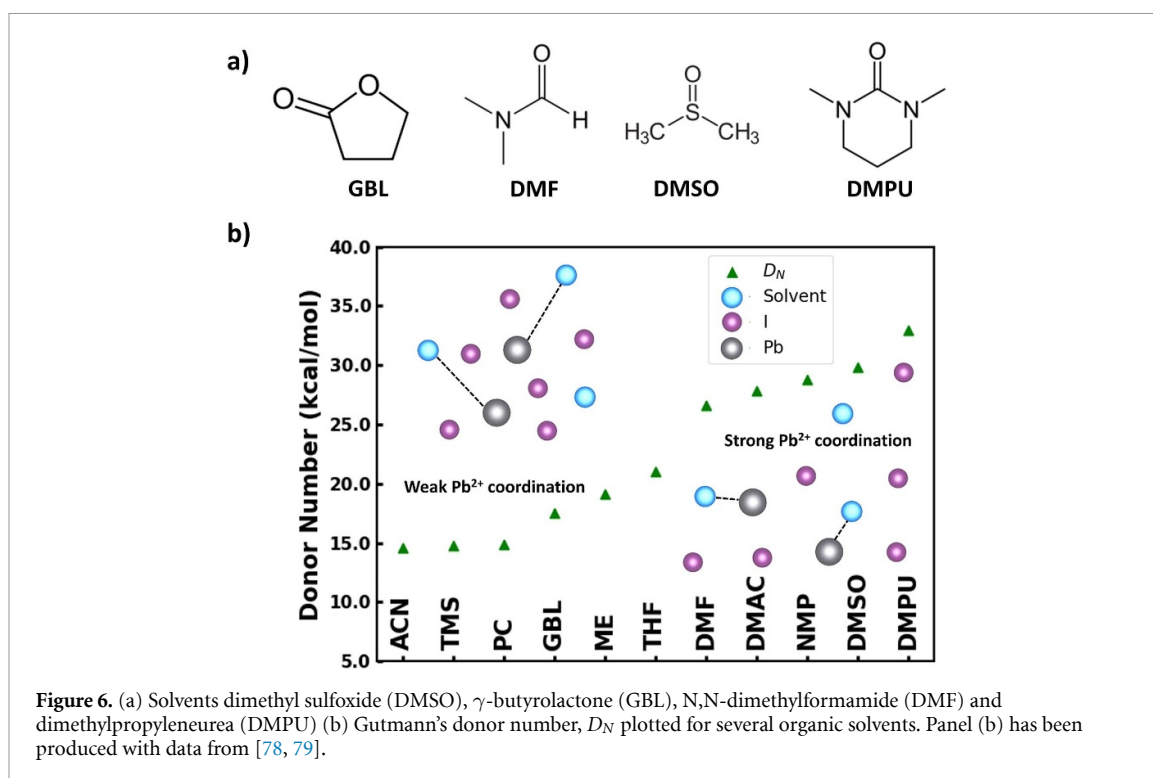
Figure 6. (a) Solvents dimethyl sulfoxide (DMSO), γ-butyrolactone (GBL), N,N-dimethylformamide (DMF) and dimethylpropyleneurea (DMPU) (b) Gutmann's donor number, D_N plotted for several organic solvents. Panel (b) has been produced with data from [78, 79].

2.4. Additive engineering

When using a solvent with a moderate Donor number (being quite volatile), such as DMF only, it is possible to improve morphology, narrow the *n*-phases distribution and obtain a preferential growth direction by the use of additives [80, 81]. These additives can stabilize the intermediate phases formed in the sol-gel stages to slow down the growth.

A common additive that is used to obtain preferential growth and an improved morphology for perovskites replacing the anion iodide or bromide is MACl [82, 83]. A thermodynamic mechanism, to explain the effect of MACl on the perovskite formation is proposed by Lehner *et al* for a 3-fluorobenzylammonium (3FBA) containing lead-iodide based perovskite (3FBA)$_2$PbI$_4$ [43]. This mechanism should be generalizable to the growth of other perovskites as well. It is proposed that MACl coordinates more strongly with the metal halide complexes present in the solution than MAI. The intermediate phase, PbI$_2\cdot$AI$\cdot$MACl$\cdot$DMF, suppresses the uncontrolled reaction of MAI and PbI$_2$ [84]. During annealing, because MACl is more volatile than MAI, it escapes from the solution. Because the evaporation happens at the liquid-air interface, a thermodynamically less stable intermediate complex, PbI$_2\cdot$AI$\cdot$DMF is now present at the surface of the solution. There the complex would align itself, most likely due to the aforementioned effect of surface tension, which leads to preferential orientation. This leads to the preferentially oriented growth of the perovskites. Also due to the slower crystallization, a larger grain size and a more smooth film morphology were obtained [85]. However, it is important to avoid adding too much MACl. If a large excess of this volatile additive is present, upon heating, the MACl in the solution will evaporate too quickly in solution, and form pinholes. The optimal ratio for a lead-iodide based perovskite is found to be MAI:MACl = 2:1.

Other additives are for example NH$_4$Cl and NH$_4$SCN salts. NH$_4$Cl increases the solubility of the metal halide complexes and can slow down the reaction in the same way as explained above for MACl. However, by using the NH$_4$SCN salt as an additive, besides forming a lewis acid-base intermediate adduct with metal halide complexes, it can also produce hydrogen bonding between the nitrogen end of SCN$^-$ and the hydrogen of NH$_3^+$ groups [86], slowing down the crystallization process even more [87]. Hence the use of NH$_4$SCN as an additive is preferred over NH$_4$Cl. However, it has also been shown that they can be used together where NH$_4$Cl produces a more compact and dense film and NH$_4$SCN can offer an improved preferential orientation to the substrate [88].

In general, additives not only coordinate with one of the precursors more strongly, but can also suppress and/or passivate defect states. For example, a lack of organic cations can leave uncoordinated metal cations and halide anions which can be passivated by additives. For example, O-donor based additives with functional groups such as C = O and S = O are frequently used as additives since these compounds

coordinate strongly with Pb^{2+} [89]. Molten salt spacers containing acetate like MAAc and BAAc have also been employed because of the strong interaction of the carbonyl group with the divalent metal cation like Pb^{2+} for the formation of $(PEA)_2(MA)_{n-1}Pb_nI_{3n+1}$ ($n = 1, 2, 3$) and $BA_2MA_{n-1}Pb_nI_{3n+1}$ ($n = 1, 2, 3, 4, 5$), respectively [90, 91]. It has been shown that when the molten salt spacer (BAAc) instead of the traditional organic spacer halide salt (BAI) is used, the colloidal size distribution becomes narrow ($\sim$0.6 nm) instead of randomly distributed from 1 nm to several micrometers. This is likely due to the strong coordination of acetate with the Pb^{2+}, which prevents the aggregation of colloids. Additionally, the formation of a pure n-phases perovskite is thermodynamically favorable when the molten salt spacer is used, whereas when a traditional spacer halide salt is used the formation of multiple n-phases is favorable.
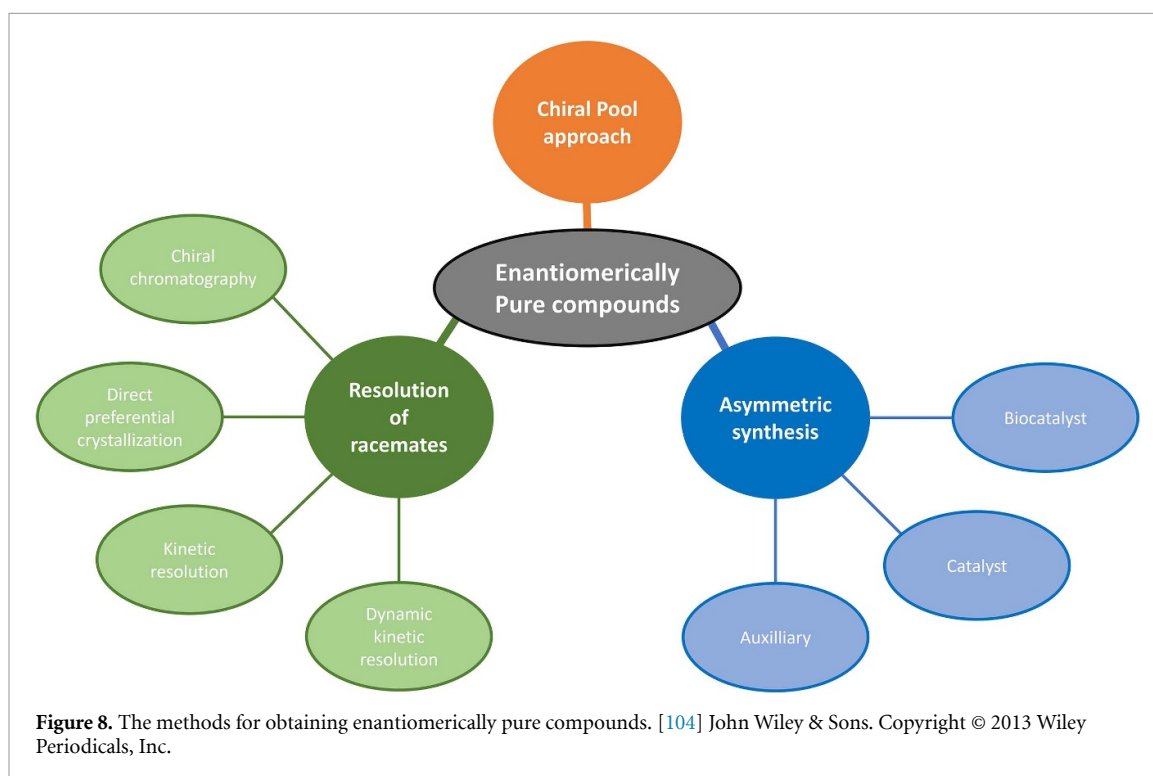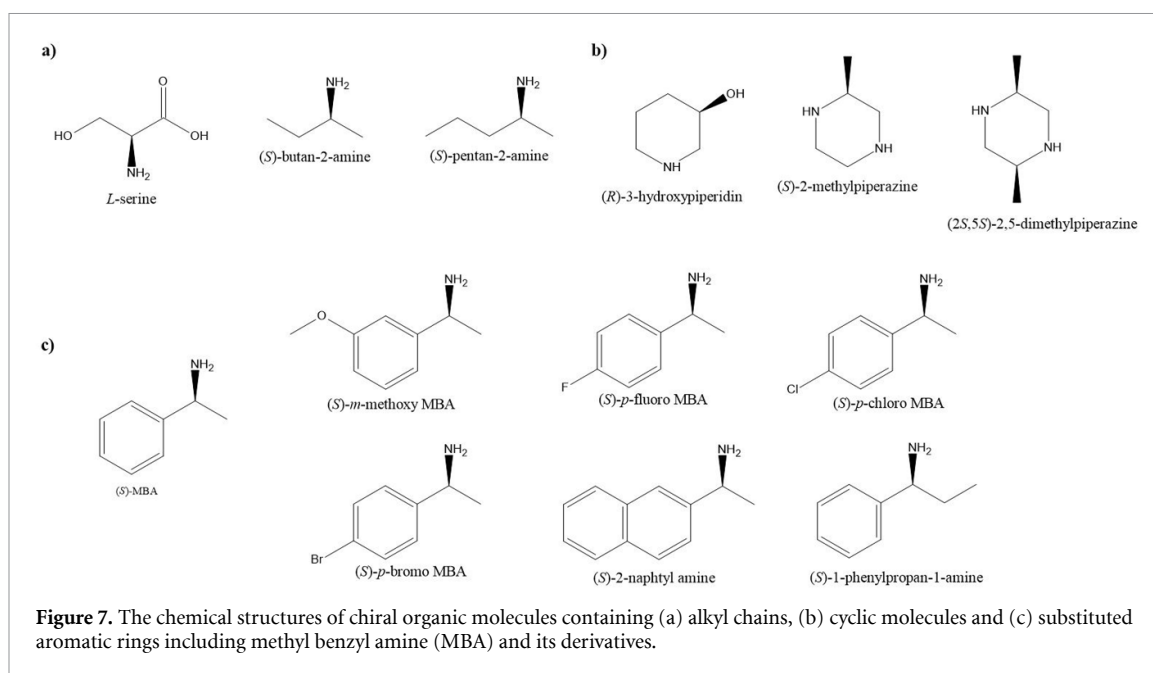
3. Growth and synthesis of chiral ligands

The transfer of chirality from the organic ligand to the inorganic framework of the halide perovskites introduces opportunities not only for novel properties, but also for the synthetic chemistry. In this section, the synthesis strategies of chiral ligands is summarized, starting with the most commonly used and commercially available ones, followed by novel ligands, such as the axially chiral molecules.

Figure 7 shows several commonly used chiral organic ligands, which of those containing alkyl chains are shown in figure 7(a) [92–94], cyclic molecules in figure 7(b) [95–97] and substituted aromatic ring in figure 7(c) [98–103]. Among these, the most widely used one is α-methylbenzylamine (MBA) due to its commercial availability. In chiral perovskites, also derivatives of MBA are frequently used of which some examples are shown in figure 7(c). Methods to obtain chiral organic molecules with high enantiomeric excess generally include the following three approaches: i) resolution of racemates, ii) asymmetric synthesis, and iii) chiral pool approach, as summarized in figure 8 [104]. The first method covers the chiral chromatography, kinetic resolution, dynamic kinetic resolution (DKR), and direct preferential crystallization. The second method uses a prochiral substrate as the starting material, which reacts with a chiral catalyst, an auxiliary or an enzyme as the chiral source. The last method, the chiral pool approach, realizes the chirality transfer to the product via the reaction of an achiral compound with an inexpensive optically active compound.

For the preparation of the most widely used chiral ligand methyl benzyl amine (MBA), many different methods can be found in the literature, including chemoenzymatic methods, enzymatic methods, and chemical synthesis. DKR of racemic MBA can yield chiral amide with high enantiomeric excess (ee) [105]. Gustafson *et al* showed the use of Pd^0-CalB CLEA bifunctional biohybrid catalyst for DKR of amines, where an aggregate of the enzyme Candida antarctica lipase B (CalB) is formed by cross-linking with glutaraldehyde (figure 9-Method A). Chemoenzymatic synthesis of MBA can also achieve high ee (93%) by conversion of amides [106] or carbamates [107], obtained from DKR of primary amines in the presence of ruthenium catalyst together with an enzyme catalysis. Here, the racemic amine was first reacted with isopropyl acetate for the former (figure 9-Method B) or dibenzyl carbonates for the latter (figure 9-Method B) in the presence of ruthenium catalyst and CalB. Both yielded chiral amines by reduction under mild conditions with full retention of configuration (figure 9-Method B).

In addition to (R)-MBA preparation (discussed above), it is also possible to obtain its (S)-enantiomer through the oxidative deamination of racemic amines by amine dehydrogenase (AmDH), which is used specifically for the oxidation of (R)-MBA to the corresponding ketone via the kinetic resolution of racemic-MBA, yielding enantiomerically pure (S)-MBA (ee>99%) [108–110]. Another example for the preparation of (S)-MBA is the formal enantioselective hydroamination of non-activated alkenes, in which an enzymatic transamination by transaminase takes place after Pd/Cu-catalyzed Wacker-oxidation of styrene derivative (figure 9-Method C) [102]. This method can be applied for the synthesis of (S)-m-methoxy MBA, (S)-p-fluoro MBA and (S)-p-chloro MBA with high yield and high ee. Xiaogen Huang showed the asymmetric synthesis of MBA derivative via the enantioselective reduction of O-benzyloxime ethers in the presence of chiral spiroborate esters (figure 9-Method D) derived from nonracemic 1,2-amino alcohols as the chiral catalyst [111]. Recently, it was shown that chiral amides [103], can be also prepared in the presence of cationic copper catalytic system, which functions in enantioselective benzylic $C(sp^3)$-H amination with peroxide as an oxidant. Here, the synthesis was carried out in the presence of CuCl, sodium tetrakis[3,5-*bis*(trifluoromethyl)phenyl]borate (NaBArF), chiral bisoxazoline ligand, and *di-tert*-butyl peroxide (DTBP) in PhCl under argon (figure 9-Method E). After obtaining chiral amides, they were deprotected with Schwartz reagent under mild conditions to yield the chiral ligand with no loss in enantiomeric purity (figure 9-Method E). Furthermore, the enantioselective preparation of MBA can be chemically achieved through the asymmetric hydrogenation of ene-trifluoroacetamides in the presence of chiral Josiphos ligands I and II, followed by the deprotection of trifluoroacetamides (figure 9-Method F) [112].

Figure 7. The chemical structures of chiral organic molecules containing (a) alkyl chains, (b) cyclic molecules and (c) substituted aromatic rings including methyl benzyl amine (MBA) and its derivatives.

Figure 8. The methods for obtaining enantiomerically pure compounds. [104] John Wiley & Sons. Copyright © 2013 Wiley Periodicals, Inc.

It should be noted that in all these above examples, the nitrogen atom was in a close neighborhood of the asymmetric centre. This comes as a requirement owing to the amino groups included in the VDW interactions. Here, the chirality plays a vital role for the formation of more ordered structure. In addition, substitution with stronger electron donor groups may enhance the electron density around nitrogen atom, leading to stronger interactions, and thus stronger hydrogen bonds. Such strategies could lead to stronger interactions, therefore, chirality transfer from organic ligands into the resulting chiral perovskites.

In addition to the organic molecules with asymmetric centres, the axially chiral molecules can be used as chiral ligands. In this special type of chirality known as the atropoisomerism, the molecule has two sets of different groups in a non-planar arrangement around a single bond, namely the chiral axis. Axially chiral biaryl compounds, such as 1,1'-bi-2-naphthol (BINOL) (figure 10(a)), 2,2'-bis(diphenylphosphino)-1,1'-binaphthyl (BINAP) (figure 10(b)), and their derivatives are one of the most studied axially chiral molecules. They were widely used as catalysts [113–115] and also starting materials [116–118] in asymmetric
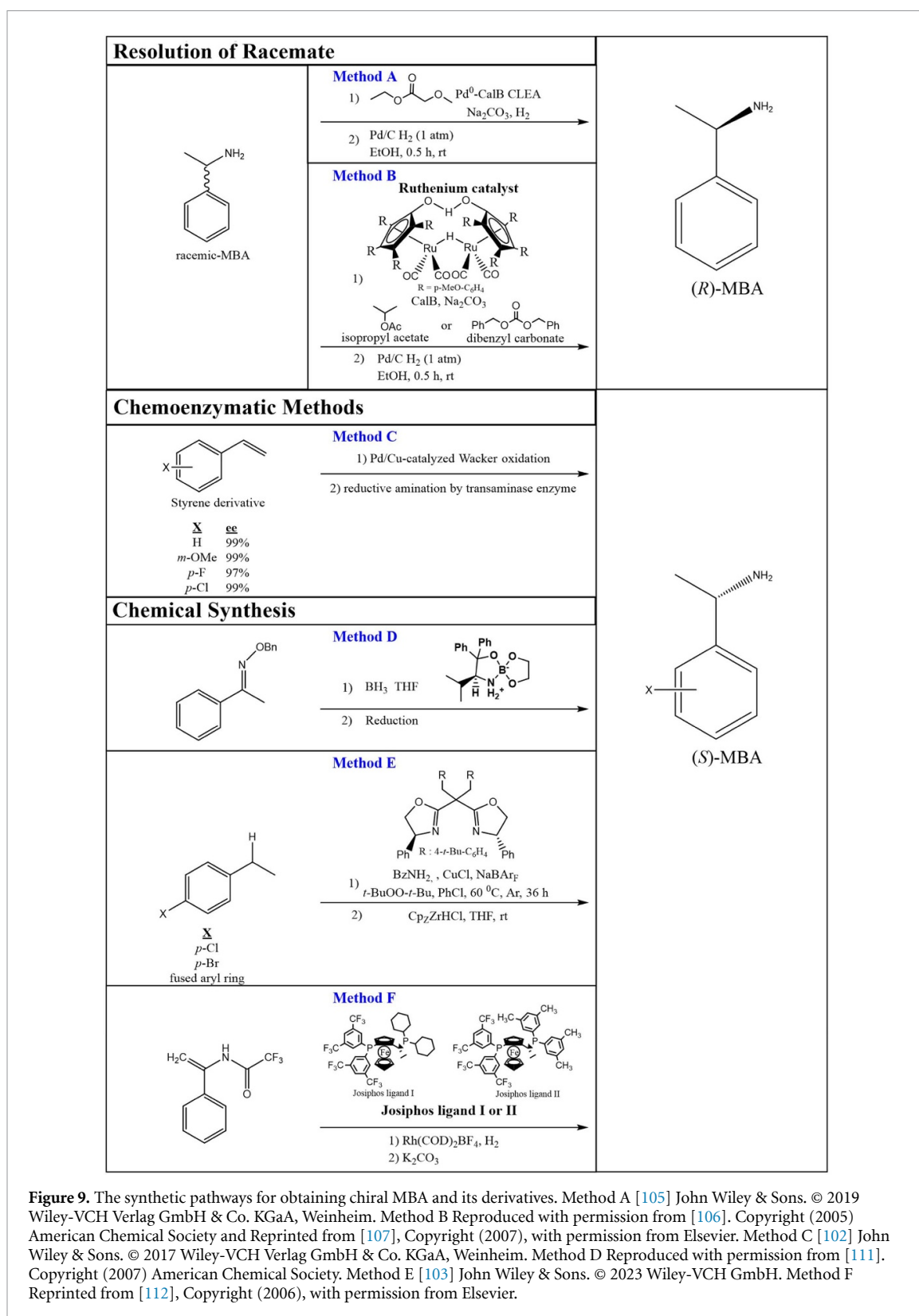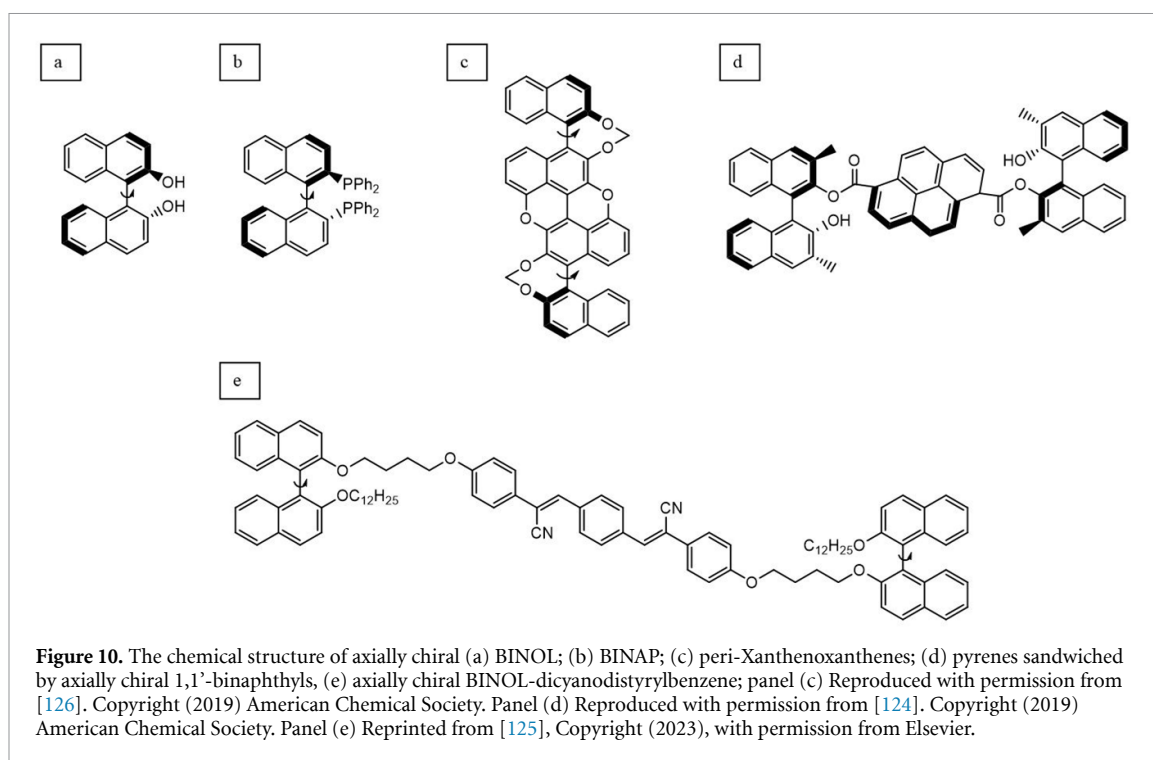
Figure 9. The synthetic pathways for obtaining chiral MBA and its derivatives. Method A [105] John Wiley & Sons. © 2019 Wiley-VCH Verlag GmbH & Co. KGaA, Weinheim. Method B Reproduced with permission from [106]. Copyright (2005) American Chemical Society and Reprinted from [107], Copyright (2007), with permission from Elsevier. Method C [102] John Wiley & Sons. © 2017 Wiley-VCH Verlag GmbH & Co. KGaA, Weinheim. Method D Reproduced with permission from [111]. Copyright (2007) American Chemical Society. Method E [103] John Wiley & Sons. © 2023 Wiley-VCH GmbH. Method F Reprinted from [112], Copyright (2006), with permission from Elsevier.

synthesis. In axially chiral molecules, the hindered rotation around the chiral axis forms non-superimposable mirror images, which can be identified if the rotation has a minimum barrier of 23 kcal mol^{-1}. It should be noted that this barrier is a function of temperature, solvent and the pH of the environment, as well as the substituents around the chiral axis [119–122], and therefore it can be modified by these parameters. The rotational barrier usually determines the stability and optical behaviour of the molecule.

Axially chiral triarylborane dyes obtained from direct borylation of commercially available enantiopure 2,2'-dimethoxy-1,1'-binaphthalene showed strong circularly polarized luminescence (CPL) activity [123]. In

Figure 10. The chemical structure of axially chiral (a) BINOL; (b) BINAP; (c) peri-Xanthenoxanthenes; (d) pyrenes sandwiched by axially chiral 1,1'-binaphthyls, (e) axially chiral BINOL-dicyanodistyrylbenzene; panel (c) Reproduced with permission from [126]. Copyright (2019) American Chemical Society. Panel (d) Reproduced with permission from [124]. Copyright (2019) American Chemical Society. Panel (e) Reprinted from [125], Copyright (2023), with permission from Elsevier.
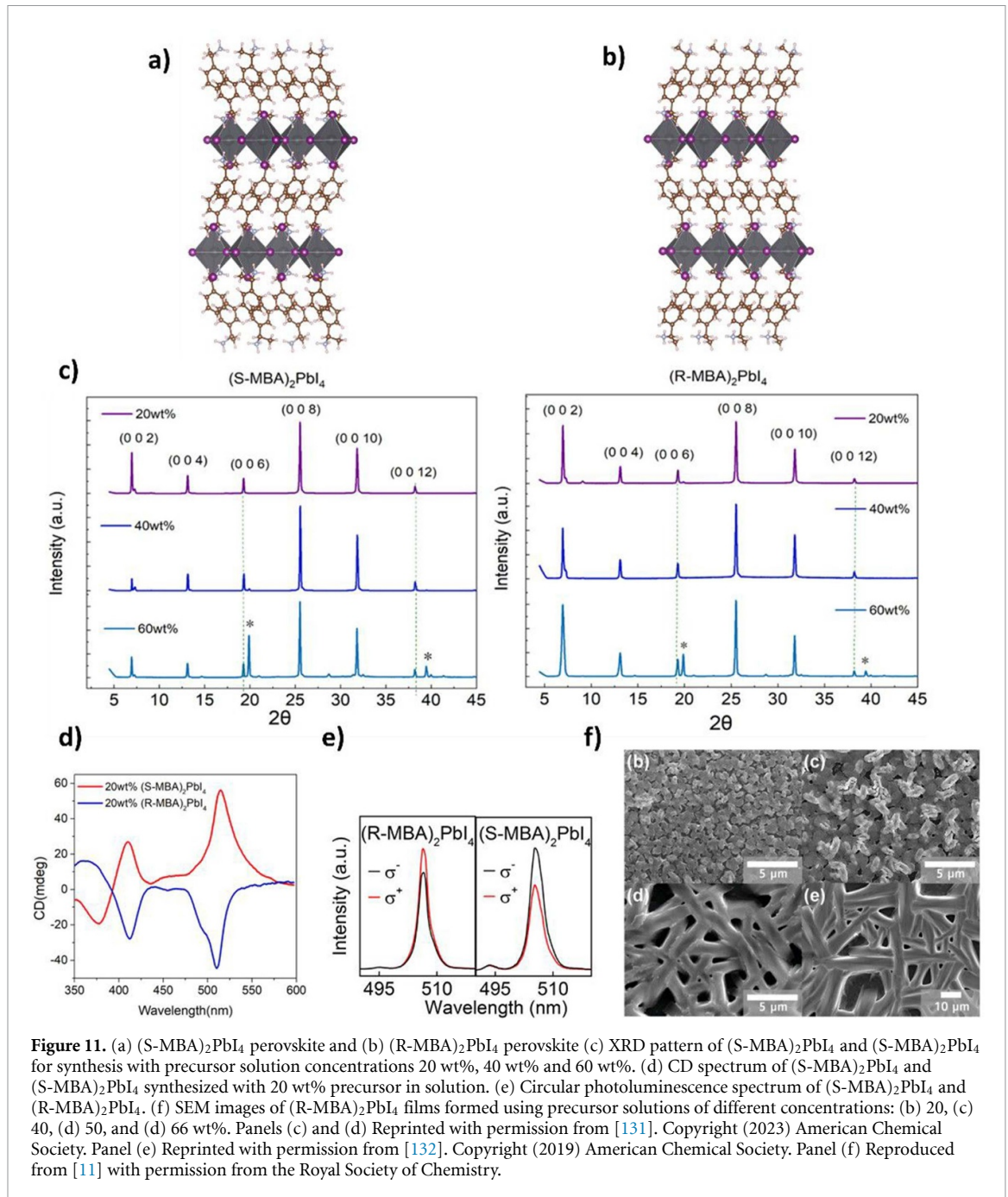
2019, Takaishi *et al* synthesized a series of axially chiral peri-xanthenoxanthenes (PXXs) from 1,1'-bi-2-naphthol without optical resolution (figure 10(c)) [126]. They found that the most rigid compound with a methylenedioxy bridge in the structure (figure 10(c)) have the highest CPL activity, concluding that the rigidity is essential for CPL activity. In the following year, the same group demonstrated the effect of solvent on the CPL activity of the pyrene derivatives sandwiched by axially chiral 1,1'-binaphthyls (figure 10(d)). (+)-CPL and (-)-CPL was detected in polar and nonpolar solvents, respectively. This finding was linked to the inversion of excimer chirality; left- and right-handed twist excimers with and without intermolecular hydrogen bonds, respectively, are formed [124]. More recently, H. Feng *et al* published the synthesis of chiral BINOL-dicyanodistyrylbenzene derivatives (figure 10(e)) having high thermal stability, photophysical properties, and CPL activity [125]. In 2021, P. Wang *et al* showed the incorporation of semiconducting helicene derivative, such as, thiahelicene and ethylenedioxythiophene with a triple axial chirality into perovskites [127]. They concluded that the doped composite film is thermally stable at $60\,^\circ$C, and is also resistant to the diffusion of mobile perovskite components, leading to a slower decomposition of perovskite. These examples demonstrate the potential of the incorporation of new molecules processing chiroptical properties, into perovskites. The more extensive exploration of available synthetic chemistry and reaction pathways are essential for the discovery of new chiral molecules, suited to be incorporated in perovskites. The fast developing field of chiral perovskites will in turn help to promote the discovery of novel synthetic chemistry for chiral molecules.

4. Growth of perovskites with chiroptical properties

4.1. Growth of chiral perovskites

A widely used strategy to obtain chiral perovskites is to introduce a chiral organic spacer into perovskites, in which a tetrahedral carbon atom is used as the chiral center. The carbon chiral center is usually terminated with an ammonium group, which directly interacts with the inorganic perovskite network, in particular, the halide species via hydrogen bonding. Such interactions play a very important role in stabilizing the chiral perovskites as well as in the transfer of chirality from the organic chiral ligand to the inorganic layers. In addition to the hydrogen bonding, as suggested by Lu *et al* [22], other interactions, such as $\pi - \pi$ stacking, C-H$\cdots\pi$ interaction in the organic components, and halogen$\cdots$halogen bonding in the inorganic layers can also stabilize the overall chiral perovskites. An example of an (*S*)-MBA$^+$ ligand and an (*R*)-MBA$^+$ ligand bonding with the inorganic perovskite network is shown in figures 11(a) and (b), respectively. Because of the wide variety of different interactions, it is difficult to get a fundamental grasp of how different structures impact morphology and the properties of the resulting perovskites. The only known requirement is that chiral perovskites must crystallize into one of the 65 Sohncke space groups because of the absence of

Figure 11. (a) (S-MBA)$_2$PbI$_4$ perovskite and (b) (R-MBA)$_2$PbI$_4$ perovskite (c) XRD pattern of (S-MBA)$_2$PbI$_4$ and (S-MBA)$_2$PbI$_4$ for synthesis with precursor solution concentrations 20 wt%, 40 wt% and 60 wt%. (d) CD spectrum of (S-MBA)$_2$PbI$_4$ and (S-MBA)$_2$PbI$_4$ synthesized with 20 wt% precursor in solution. (e) Circular photoluminescence spectrum of (S-MBA)$_2$PbI$_4$ and (R-MBA)$_2$PbI$_4$. (f) SEM images of (R-MBA)$_2$PbI$_4$ films formed using precursor solutions of different concentrations: (b) 20, (c) 40, (d) 50, and (d) 66 wt%. Panels (c) and (d) Reprinted with permission from [131]. Copyright (2023) American Chemical Society. Panel (e) Reprinted with permission from [132]. Copyright (2019) American Chemical Society. Panel (f) Reproduced from [11] with permission from the Royal Society of Chemistry.

rotational and inversion symmetry [128]. After crystallization of a chiral perovskite in one of these space groups, one can assess the degree of chirality it exhibits. Whereas the chiral perovskite shows different symmetries with respect to an achiral perovskite, these differences cannot be observed in x-ray diffraction (XRD) patterns since the crystallographic orientation does not change drastically, as can be seen in figure 11(c). To identify whether a material exhibits chirality one either needs to measure the circular dichroism (CD) spectrum, of which an example is shown in figure 11(d), or circular polarized photoluminescence (CPPL) of which a spectrum is shown in figure 11(e). These quantities represent the differential absorbance and emittance of CPL, respectively. The degree of chirality, is determined either by the luminescence anisotropy factor, g_{lum}, or the absorbance anisotropy factor, g_{abs}, which describe the normalized difference luminescence intensity or absorbance of left- and right-CPL, respectively, with values ranging from -2 to 2 [129, 130]. Hence, an important relation in chiral perovskites is the relation between the anisotropy factor, g, and the microscopic crystal structure.

With this in mind, in the following paragraphs, strategies for the growth of chiral perovskites are discussed, with the aim of correlating the anisotropy factor (g) with their microscopic structures, like dimensionality, atomistic structures, morphology, etc.

Crystallographic orientation plays an important role in the g factor of chiral perovskites. This has been systematically demonstrated by Ahn *et al* whom studied the properties of both (*S*-MBA)$_2$PbI$_4$ and (*R*-MBA)$_2$PbI$_4$ synthesized at varying conditions [11]. Perovskite films with different thicknesses and morphologies were obtained by spin-coating a precursor solution with varying concentrations of 20, 40, 50, and 66 wt% dissolved in DMF under the same spin-coating conditions. First of all, this yields different crystallinities of the films as is shown in the scanning electron microscopy (SEM) images, figure 11(f), for an (*R*-MBA)$_2$PbI$_4$ film. For higher precursor concentrations of 50 and 60 wt%, needle-like crystals are formed whereas for a lower concentration of 20 wt% the crystals are planar. The morphology of the 40 wt% crystal exhibits properties of both the lower and higher precursor concentration with an underlying planar crystal structure as well as some embedded needles coming out of this plane. Next to this, the crystallographic orientation of the films also changes with different precursor concentrations in the solution. For the 20 wt%, the crystal was oriented along the (0 0 2) plane, but once the concentration is increased to 40 wt% also a peak corresponding to the (0 2 0) plane is observed. For the films synthesized with the highest concentration of precursors the films were preferentially oriented along the (0 2 0) plane. The effect of using different precursor concentrations was also investigated recently by Hu *et al* for the synthesis of (*S*-MBA)$_2$PbI$_4$ and (*R*-MBA)$_2$PbI$_4$ [131]. Hu *et al* used precursor concentrations of 20, 40 and 60 wt% in DMF to synthesize the thin films and XRD patterns are shown in figure 11(b). The same results are found here as in the work by Ahn *et al*.

The tunable growth orientation as described above has also been shown to impact the CD signal [133]. Scalon *et al* recently synthesized (*R*-, *S*- and rac-MBA)$_2$PbI$_4$ perovskites using two different solvents, DMF and acetonitrile (ACN) [134]. The oxygen in DMF has a more basic character than the nitrogen in ACN and therefore it allows for stronger interaction with hydrogen bond donors, such as R'-NH$_3^+$ and the lewis acidic Pb^{2+}. As discussed in the previous section, due to the difference in interaction of the solvents with precursor materials, the crystallization pathway can change, impacting the final phase composition and growth orientation of the film. In the same study, no intermediates are identified in the formation of the 2D perovskite, but a 1D phase is observed in both samples regardless of the choice of solvents. However, less 1D phase is present in the DMF-based films than the ACN based films. Also it is observed that after thermal annealing, both films show the same out of plane orientation for the 2D perovskite phase, but the orientation of the ACN samples is more pronounced. The orientation of the 1D phase was less dependent on the solvent. Since the ACN treated sample shows both an improved out of plane orientation and a more pronounced 1D phase, a higher anisotropy factor is observed for this sample compared to the DMF sample.

A solvent modulation strategy was also employed by Zhu *et al* to increase the circularly polarized photoluminescence performance of a (*S*- and *R*-MBA)$_2$PbI$_4$ perovskite and CdSe/ZnSe quantum dot (QD) composite [135]. Compared to N,N-dimethylformamide (DMF), dimethyl sulfoxide (DMSO) and N-methylpyrrolidone (NMP) slow down crystallization of the chiral perovskites, because of a stronger coordination ability, allowing for (0 0 2)-plane oriented growth instead of (0 2 0)-plane. In addition to the growth orientation, solvent modulation also yields significantly enlarged grain sizes with an average value of 21 μm for the DMF sample to 37 μm for DMSO and 57 μm for NMP. The significant increase in grain size compared to DMF can be ascribed to the stronger coordination ability of DMSO and NMP with precursors which slows down growth. However the increased grain size of the NMP sample compared to the DMSO sample can also be attributed to the fact that NMP exhibits the largest steric hindrance, which delays intermolecular interactions between precursors and yields a more stable nucleation environment, such that there is sufficient time for the perovskite grains to grow [136]. These changes in morphology impact the degree of chirality in the chiral perovskite. The luminescence anisotropy factor, g$_{lum}$, is increased over 4 times, with the original sample with DMF as solvent having a factor of 1.53×10^{-3} to a value of 2.45×10^{-3} for DMSO and finally a factor of 6.91×10^{-3} for NMP.

In this section up until now the synthesis of (*S*- and *R*-MBA)$_2$PbI$_4$ chiral perovskites has been discussed, but because of their compositional flexibility, a large family of chiral perovskites can be designed. For example, in the inorganic perovskite network alone, a broad variety of metals have been used. The most frequently used metals are lead [137] and tin [138]. These two metals have a very similar electronic structure, with both Pb^{2+} and Sn^{2+} having a stereochemically active, non-bonding, lone pair in the 6 s^2 and 5 s^2 shell, respectively [139]. The stereochemical activity typically increases with decreasing size of the cations, which is in line with the increasing covalent character of the elements, and this activity causes interesting features in 3D perovskites as reported by Fabini *et al* [140]. This lone pair activity also causes structural distortions of the individual octahedra due to the lone pair repelling the halide anions as reported by Tao *et al* in the synthesis of the 1D perovskite (*R/S*-α-PEA)SnX$_3$ (X = Cl, Br) [141]. The distortions caused by the lone pair lead to a reduction of symmetry in the crystal, and the asymmetric hydrogen bonds from the chiral cations introduce additional asymmetry into the inorganic framework. In 2D perovskite it is noted by Lu *et al* that the structural distortion of the inorganic octahedra in (MBA)$_2$SnI$_4$ is significantly larger than the distortion

in (MBA)$_2$PbI$_4$ [142]. A recent work by Fortino *et al* based on *ab initio* calculations does show that the electronic coupling between the MBA ligand and tin-octahedra is stronger than with lead-octahedra [143]. This large electronic coupling stems from the different assembling of the chiral ligands in the tin-based perovskite, resulting in a highly distorted coordination allowing for CH$\cdots\pi$ interactions.

The lone-pair activity increases even more when considering Ge-based chiral perovskites and it leads to an even more increased distortion than in Sn-based perovskites as reported by Li *et al* [144]. Thus the ns^2 lone-pair electrons of group IV-cations and its stereochemical activity show a strong effect on the perovskite crystal structure. However, one may note that due to the smaller size of Ge with respect to Sn and Pb, some organic cations, such as MA or FA, may become oversized for the perovskite cages. Also the penetration depth of organic cations into the inorganic cages is reported to be smaller in the 2D perovskite (4Br2FBZ)$_2$Ge$_2$I$_4$ ($n = 1$) than their Sn- and Pb-based counterparts [145]. In the case of $n = 1$, the GeI$_6$ octahedra can tilt unrestrictedly, and the octahedra's themselves do not distort. However when the dimensionality is increased to $n = 2$, (4Br2FBZ)$_2$CsGe$_2$I$_7$, the terminal iodides are now restricted to preserve the perovskite structure. To accommodate for the 4Br2FBZ, the outer iodides must move, but the inner iodides cannot move, leading to the significantly distorted octahedra's.

Another metallic compound used in chiral perovskites with a strong lone-pair expression is the trivalent cation Sb^{3+}, and these antimony based perovskites typically crystallize into 0D- or 1D-perovskites [146–148]. It was recently shown by Chen *et al* that since trivalent Sb^{3+} has its lone pair electrons and is thus prone to structural distortion, the perovskite (TMA)$_3$Sb$_2$X$_9$ (TMA = NH(CH$_3$)$_3^+$, X = Cl,Br), forms a non-centrosymmetric structure due to the TMA-induced hydrogen bonding [149]. This is a 0D chiral perovskite where the distortions of the Sb$_2$Br$_{10}$ dimers are caused by the stereochemical activity of the Sb 5 s^2 electrons. One may also consider a Bismuth based chiral perovskite. As shown by Maughan *et al* the lone pair on Bi^{3+} yields octahedral distortions in MBA$_4$Bi$_2$X$_{10}$ (X = Cl$^-$,Br$^-$) and the MBA causes a helical arrangement of the 1D edge-sharing Bi$_2$X$_{10}$ dimers [150].

Chiral perovskites without these lone-pair effects can also be synthesized by using transition metals such as Mn [151], Fe [152], and Cu$^+$ or Cu^{2+} as a metal for example [153–156]. An often studied Cu-based chiral perovskite is 0D (*R*-/*S*-MBA)$_2$CuCl$_4$ [157]. However, more interestingly, Dibenedetto *et al* reported on the synthesis of the novel 0D (R-/S-ClMBA)$_2$CuCl$_4$ compound where its racemic compound crystallizes into a 1D structure [158]. The racemic material crystallizes with a (ClMBA)CuCl$_3$ stoichiometry in a centrosymmetric structure and it is composed of Cu$_2$Cl$_6^-$ dimers coordinated with 5 Cu^{2+} ions in infinite chains.

Another transition metal that has been used in chiral perovskites is Co. Ultrasmooth (NEA)$_2$CoCl$_4$ were synthesized by Wang *et al* using the additive tris(8-oxoquinoline)aluminum(III) (Alq$_r$) [159]. This additive acts as a nucleating agent and has the ability to flexibly interact with (NEA)$_2$CoCl$_4$ crystalline grains in different orientations as the aromatic structure of the quinoline ring is analogous to the NEA molecule and allows for $\pi - \pi$ stacking in several directions.

Next to the structural changes in chiral perovskites upon a change in the metal cations, it has been shown to impact the CD signal as shown in figure 12(a) for Sn-concentrations ranging from 0% to 100% in a (*S*- and *R*-MBA)$_2$Pb$_{1-x}$Sn$_x$I$_4$ chiral perovskites synthesized by Yao *et al* [160]. It can be observed that samples with Sn-concentrations of 5% and 10% show high CD values comparable to their Pb analogue but for higher Sn-concentrations the CD signal decreases. From the obtained films, CPL detectors are fabricated and the photocurrent anisotropy factor is calculated to be up to values of 0.44 for (*S*-MBA)$_2$Pb$_{0.9}$Sn$_{0.1}$I$_4$, compared to 0.18 for its lead analog. One may also note that the anisotropy factors of the photocurrent are significantly higher than the absorbance anisotropy factors. This could be attributed to CISS, as proposed by Lu *et al* [142].

Also using Sn based perovskites as an example, it was noted by Lu *et al* that the octahedral distortion of (MBA)$_2$SnI$_4$ is among the largest of reported Sn based layered perovskite structure in literature as shown in figure 12(b). This same figure shows that the octahedral distortion of the chiral perovskites is highly dependent on the chosen chiral ligand. Apart from changing the chiral ligand to introduce a different degree of distortion, one can also dope a layered chiral perovskite with another chiral ligand to get a mixed chiral cation system. This is done by Xie *et al* by taking (*S*-BrMBA)$_2$PbI$_4$ (*S*-BrMBA = (*S*)-(-)-4-bromo-α-methylbenzylammonium) and dope it with a small amount (<10%) of *S*-2-MeBA (*S*-2-MeBA = (*S*)-(-)-2-methylbutylammonium). Doping the chiral perovskite yields a change in structural symmetry from a higher symmetry (C2) to the lowest symmetry (P1) at a doping concentration of ~4%. At this concentration a rearrangement of the *S*-BrMBA cations is facilitated, which shifts the Pb and I atoms from their original positions and causes an additional degree of asymmetric distortion in the inorganic layers. As a result of this extra degree of asymmetric distortion, it is shown by DFT calculations that spin-splitting along different k-paths can be modulated.

Instead of doping a chiral perovskite with other chiral ligands, one may also include both achiral and chiral cations in the synthesis. Heindl *et al* introduced an enantiomerically pure amino acid (*S/R*)-ABA
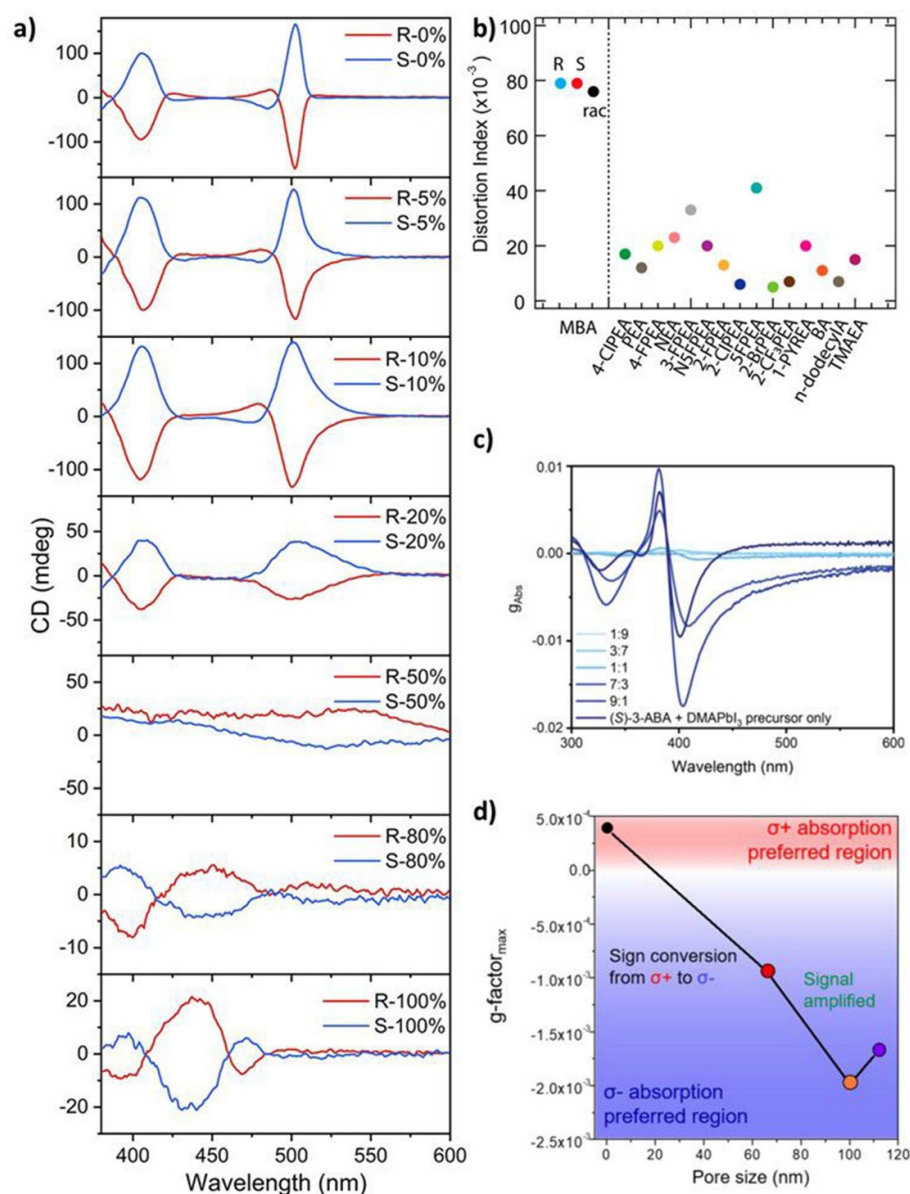
Figure 12. (a) CD spectra of (*S*- and *R*-MBA)$_2$Pb$_{1-x}$Sn$_x$I$_4$ for $x = 0$, 0.05, 0.1, 0.2, 0.5, 0.8 and 1. (b) Bond length distortion indices of (rac-, *S*- and *R*-MBA)$_2$Sn$_x$I$_4$ compared to those of other layered Sn-I perovskites. (c) Chiroptical properties of (S)-3-ABA functionalized DMAPbI$_3$ via added amino acid content. (d) Plot of local maximum g-factor at the first extinction band edge as a function of AAO pore sizes. Panel (a) Reprinted with permission from [160]. Copyright (2023) American Chemical Society. Panel (b) Reprinted with permission from [142]. Copyright (2020) American Chemical Society. Panel (c) [161] John Wiley & Sons. © 2022 The Authors. Advanced Optical Materials published by Wiley-VCH GmbH. Panel (d) Reproduced from [164]. CC BY 4.0.

(3-aminobutyric acid) into the synthesis of 1D dimethylammonium lead iodide (DMAPbI$_3$) [161]. The 1D chain structure of DMAPbI$_3$ is maintained with the introduction of (*S/R*)-3-ABA and no new bulk chiral crystal phase is formed. It is proposed that the origin of the chiroptical signal arises from chirality transfer via surface interactions from the amino acid to the DMAPbI$_3$. To test this hypothesis, films are fabricated under different synthesis conditions. For example, the spin-coating time is varied from 20 s to 100 s. It is observed that the CD signal is weaker for the 100 s spin coated film than for the 20 s one. This could be explained by a decreased surface-to-bulk ratio for the 100 s spin-coating film and thus this supports the idea of chirality transfer on the surface. Hence, to optimize the surface-to-bulk ratio, films with smaller grains are beneficial for obtaining a stronger chiroptical signal. Therefore, the nucleation rate should be maximized whilst grain coarsening should be suppressed, which can be achieved by optimizing for example the spin-coating time, the precursor concentration, the solvent mixture and the annealing temperature. The (*S*)-3-ABA -concentration dependent CD signals can be seen in figure 12(c). It can be observed that for low concentrations of the amino acid almost no CD signal is observed whereas upon increasing this concentration a maximum CD signal is

obtained between a 7:3 and a 9:1 ratio of the (S)-3-ABA/DMAPbI$_3$:DMAPbI$_3$ precursor solution mixing ratio. The maximum value obtained for the absorbance anisotropy factor is g$_{abs}$ = 1.75×10^{-2}, which exceeds the previously mentioned value of (R/S)-MBA$_2$PbI$_4$ by one order of magnitude, making this material promising for the detection of CPL.

Above discussion summarizes the use of achiral together with chiral ligands to induce chirality. Another chiral induction strategy, where the chiral inducer is not incorporated in the final product, was employed by Zheng *et al* to construct a series of chiral perovskites, DMA$_4$MX$_7$ (M = Sb or Bi, X = Cl or Br) [162]. The chiral inducer that was used during synthesis was R/S-2-MPD (MPD = methylpiperidine), and the formed crystals were in a chiral structure rather than an achiral one. The chirality is purely caused by the [MX$_6$]$^{3-}$ octahedron distortions in such a way that these are helically organized. During synthesis, two intermediates were formed. One is formed when the chiral inducer is added before the DMA precursor. This yields the formation of one R/S-2-MPD$^+$ and a distorted asymmetric [MX$_6$]$^{3-}$ octahedron in a formula of the form of (S-2-MPD)$_3$BiBr$_6$. A second intermediate is formed when DMA precursor is added, with the formula [(S-2-MPD)(DMA)]BiBr$_5$ and it crystallizes in the same space group as the final chiral compound DMA$_4$BiBr$_7$, but without the chiral inducer present. In this intermediate, the metal halide octahedra form a corner-shared zigzag chain and are distorted due to the N-H$\cdots$Br hydrogen bonds and coulomb interactions from the surrounded S-2-MPD$^+$ and DMA$^+$ cations. In addition, to Sn and Bi based chiral perovskites, using the similar induction process, Guan *et al* synthesized In-based ones, i.e. DMA$_4$[InCl$_6$]Cl and DMA$_4$[InCl$_6$]Br single crystals using R/S-NEA as chiral inducer [163]. The substitutions from Cl to Br leads to the induction of centimeter-scale single crystals and a significant change in the octahedral distortions.
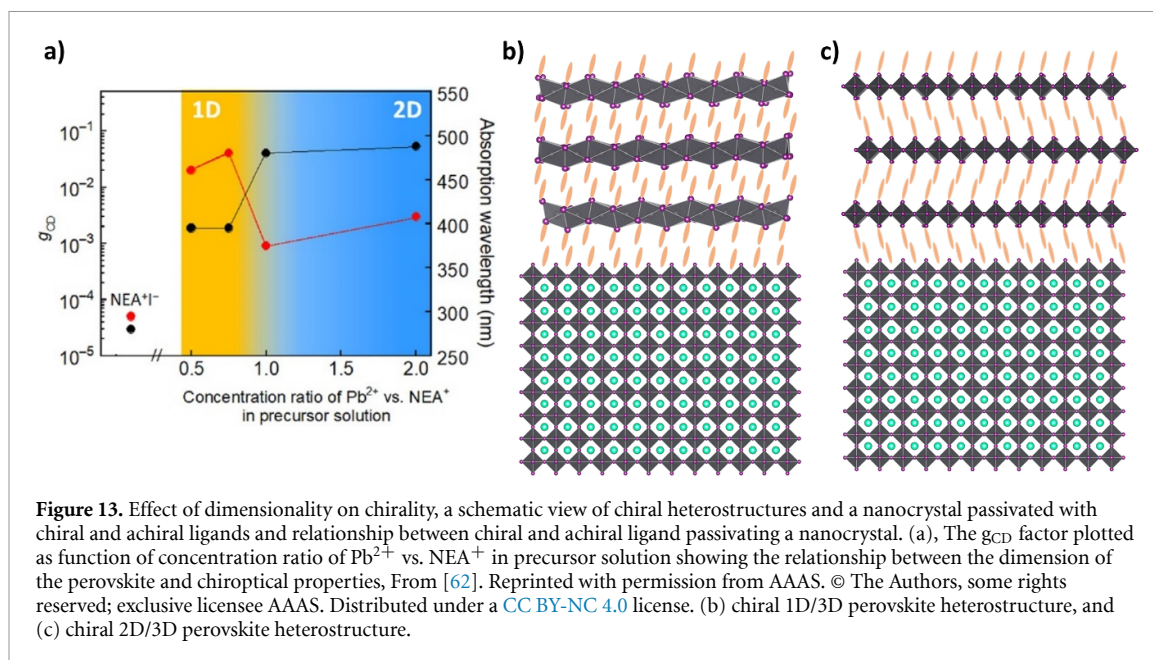
Finally, strain engineering has also been used to tune the structural chirality of perovskites. Ma *et al* did so by growing strained MBA$_2$PbI$_{4(1-x)}$Br$_{4x}$ in nanoporous anodized aluminium oxide (AAO) templates with varying pore sizes [164]. Firstly, a composition with a specific halide composition ($x = 0.325$) is chosen, being the composition at which the phase transitions from the iodide to the bromide determinant phase. The achieved maximum absorbance anisotropy factor, g$_{max}$, shown in figure 12(d) is an about 5-fold improvement in g$_{max}$ from a planar grown chiral perovskite to one grown in a 100 nm pore-size template of AAO. DFT calculations show that the induced micro-strain by the template can amplify the asymmetric behavior of hydrogen bonding between the chiral organic molecule and the inorganic framework. This can promote chirality transfer by increasing the chiral distortion in the inorganic framework. It is suggested that the chiroptical activity is more amplified by the asymmetric hydrogen bonding between MBA cations and the inorganic framework than the structural distortion in the lead halide framework itself.

Apart from compositional engineering of chiral perovskite, the dimensionality of the chiral perovskite can also affect the degree of chirality. It has for example been determined that 2D chiral perovskites with a lower n-phases show a stronger degree of chirality than those with a higher n-phases [165, 166]. Next to this, a lower dimensionality of the chiral perovskite tends to yield a higher degree of chirality as shown in figure 13a [62]. Therefore, tuning the molar ratio of chiral to achiral components in the perovskites can impact the anisotropy factor greatly.

4.2. Introduction of chirality into 3D perovskites

Lower dimensional chiral perovskites do not fully harness the optoelectronic properties in the perovskites due to the insulating organic spacer cations. 3D chiral perovskite containing a chiral A cation have recently been synthesized by Ju *et al* in the form of (R-3AP)RbBr$_3$ [13]. In this material, a larger alkali metal framework is formed, accommodating larger organic cations compared to Pb- or Sn-based structures. However, recent progress by Chen *et al* has led to the synthesis of 3D chiral MAPbBr$_3$ perovskites, achieved without introducing chiral ligands [167]. These crystals are synthesized in solution by an inverse temperature crystallization method with the addition of micro- or nanoparticles with a tetragonal phase as nucleating agents. This tetragonal phase is also found in MAPbBr$_3$ grown on these particles, which restricts the rotational freedom of the MA by enhancing the H-bonds between MA$^+$ and the surrounding halogen atoms. However, the MA$^+$ in the cubic perovskite phase is free to rotate. During the growth, although particles keep doping the MAPbBr$_3$ crystals, autocatalytic chiral growth takes over the growth process, meaning that the growth of the next perovskite layer on the growth front, favors the same handedness as that of the growth front. This is how the crystal becomes chiral overall. The handedness of the crystal, and thus its chirality, stems from the chiral orientation patterns of the MA$^+$, made possible by the tetragonal phase, along with its structural and electronic hybridization with the inorganic framework to form chiral supercells. A major challenge here is the full control over the handedness selectivity during crystal growth.

However, there are other more straightforward ways to introduce chirality into 3D perovskites. One can for example introduce chirality on the surface of a 3D perovskite, either by templating it with chiral ligands or by growing a chiral low-dimensional perovskite thin film on the surface. Typically, this is done in

Figure 13. Effect of dimensionality on chirality, a schematic view of chiral heterostructures and a nanocrystal passivated with chiral and achiral ligands and relationship between chiral and achiral ligand passivating a nanocrystal. (a), The g_{CD} factor plotted as function of concentration ratio of Pb^{2+} vs. NEA^+ in precursor solution showing the relationship between the dimension of the perovskite and chiroptical properties, From [62]. Reprinted with permission from AAAS. © The Authors, some rights reserved; exclusive licensee AAAS. Distributed under a CC BY-NC 4.0 license. (b) chiral 1D/3D perovskite heterostructure, and (c) chiral 2D/3D perovskite heterostructure.
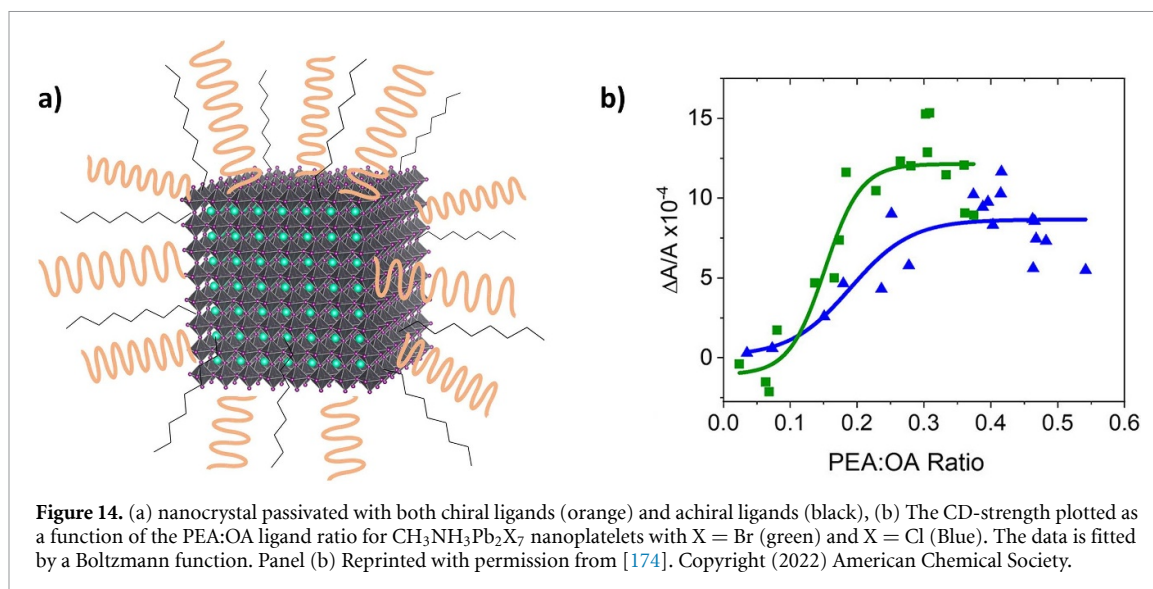
nano-systems, such as heterostructures at the nanoscale (figures 13(b) and (c)), maximizing the chirality transfer because of their high surface to volume ratios.

4.2.1. Chiral patterned NCs
Patterning perovskite nanocrystals with organic ligands plays a crucial role in their stability and surface passivation, but one can also use it to include chiral features by using chiral ligands [168]. Such a nanocrystal passivated by both chiral and achiral ligands is shown in figure 14(a). The chirality in nanocrystals patterned with chiral ligands not only arises from the chiral ligands, but from the perovskite nanocrystal itself as well. It has been shown by Luther *et al* by the fabrication of chiral (*R*-, *S*-MBA):Br treated $CsPbBr_3$ nanocrystals. DFT calculations suggest that the outermost layers of lead bromide octahedra are distorted [169], which is a sign of the chirality transfer from the chiral ligands to the nanocrystal. Since this is a surface phenomenon, a high surface to volume ratio is desired to obtain a high degree of chirality in the system. Therefore, chiral perovskite nanoplatelets are frequently employed [98, 170]. However, since the chirality is induced only on the surface, these systems show a relatively weak chiroptical signal compared to chiral perovskites having a chiral crystalline structure due to the incorporation of chiral ligands in the perovskites [171–173]. As a result of this, it is important to understand how to introduce as much chirality as possible in the nanocrystals. Therefore, one important point to consider is what surface coverage of chiral ligands leads to the most chirality in the nanocrystal. Waldeck *et al* studied this both computationally and experimentally for a $MAPbX_3$ nanoplatelet covered with chiral PEA ligands and achiral OA ligands on the surface, and found a non-linear relationship between chiroptical properties and surface coverage of chiral ligands of which the results are shown in figure 14(b) [174].

This non-linear relationship suggests that the chiral imprinting of the ligand on the nanocrystal saturates at high chiral ligand concentrations. In other studies it has been found experimentally that there is a ratio of chiral ligands to achiral ligands on the nanocrystal surface for which the maximum chiroptical signal is reached, and thus no saturation is observed [175, 176]. Also Hubley *et al* found in a study of a $MAPbBr_3$ nanocrystal treated with several chiral ligands that a too high or too low of a molar fraction of chiral to achiral ligands leads to a decrease in the chiroptical signals [177]. The explanation for this result is that when too few chiral ligands are adsorbed on the surface, there is too little chirality induced in the crystal, just like in the aforementioned model by Waldeck *et al*. For the case where the surface coverage of the chiral ligands is too high, it is observed that the formation of polydisperse thicknesses and different ligand binding orientations yield a decrease in the chiroptical signals. In this study by Hubley *et al* it is also shown that minor structural changes in the ligand result in significant changes in both magnitude and sign of the CD signal. It is for example shown that adding a methyl group on the para-position of MBA yields a significant increase in CD signal. Hence to optimize the magnitude of the chiroptical signal, care must be taken with both the choice of chiral ligand and the molar ratio of chiral ligands and achiral ligands.

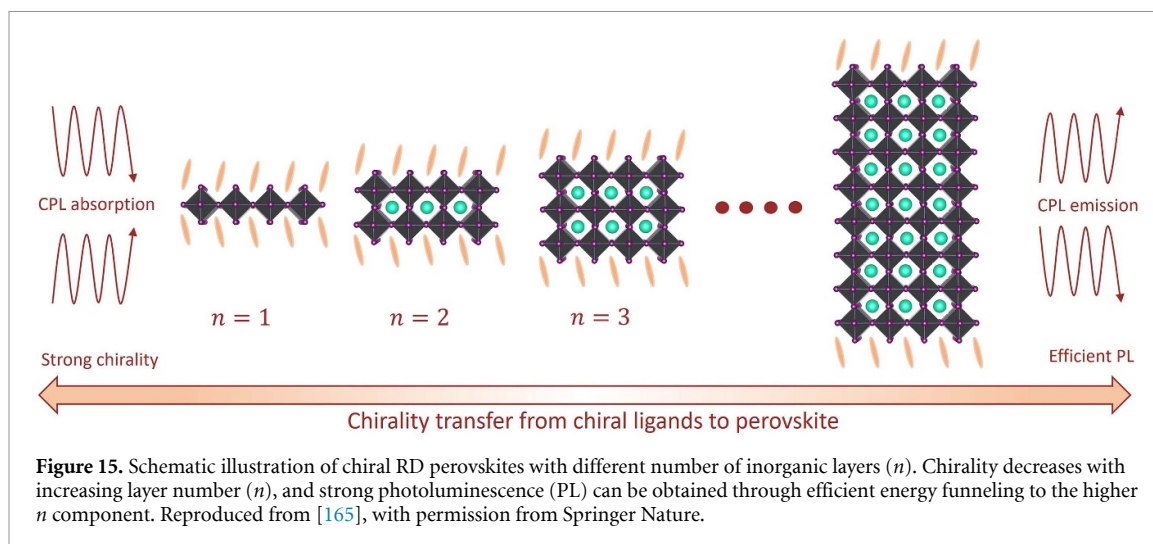**Figure 14.** (a) nanocrystal passivated with both chiral ligands (orange) and achiral ligands (black), (b) The CD-strength plotted as a function of the PEA:OA ligand ratio for $CH_3NH_3Pb_2X_7$ nanoplatelets with X = Br (green) and X = Cl (Blue). The data is fitted by a Boltzmann function. Panel (b) Reprinted with permission from [174]. Copyright (2022) American Chemical Society.

4.2.2. Chiral heterostructure

Like chiral patterned perovskite nanocrystals, also combining a low dimensional perovskite and a 3D perovskite nanocrystal can increase stability and passivate the surface [178]. These low dimensional perovskites can be made chiral, such that both the features of the 3D perovskites and the chiral low dimensional perovskites are combined. A schematic view of both a chiral 1D/3D and a 2D/3D perovskite heterostructure are shown in figures 13(b) and (c), respectively.

The growth conditions are crucial to obtain the desired heterostructure. In a recent work by Huang *et al* it was shown that for a $MAPbI_3$ crystal treated with a chiral MBA cation at the interface, the formation of a 2D layer can be triggered and that the dimensionality of this layer can be tuned from 2D to 1D by changing the thermal annealing temperature [179]. A lower annealing temperature of 50 °C leads to the 2D/3D heterostructure whereas a higher annealing temperature of 100 °C leads to a 1D/3D heterostructure irrespective of whether *R*-, *S*-, or racemic (rac) MBA was used. Next to the temperature changing the dimensionality of the chiral perovskite, one also has to take into account that the substrate, $MAPbX_3$ (X = Cl^-, Br^-, I^-), can decompose already at moderate temperatures and thus care should be taken [180]. Finally, one can also first grow a chiral perovskite and template this with a 3D perovskite. This is done by Zhang *et al* for two lead iodide based 2D perovskites containing either *R*- or *S*-methylphenethylammonium cations, $(R-, S-MPEA)_2MAPbI_2I_7$, which are templated with $MAPbI_3$ [181]. The heterostructure is grown using a 2-step method. Firstly the 2D perovskite is grown by starting in a stable unsaturated HI solution, and then lowering the temperature by 2 °C per day to bring the solution slowly to a saturated state to promote growth. The second step is to dip the 2D perovskite crystal into this supersaturated solution, which gives the quick epitaxial growth of a $MAPbI_3$ layer. If not in the supersaturation region, the 2D perovskite crystal surface can be etched or it can lead to the formation of a second phase. The key to this method for heterostructure synthesis is the spontaneous nucleation of the $MAPbI_3$ on the $(R-, S-MPEA)_2MAPbI_2I_7$ crystal surface, which can be controlled by the $MAPbI_3$ concentration and dipping time.

4.3. Existing and new functionalities of chiral perovskites

Chiral materials, and thus chiral perovskites, do not require any additional optical elements to emit or detect CPL. Therefore, they have great potential in integrated devices for 3D displays, quantum computing and bio-imaging. To be useful as a CPL photodetector, chiral materials need to have both a high CPL absorption, thus a high degree of chirality, and also effective charge transfer. Hence, chiral perovskites are promising materials for CPL photodetectors. Several CPL photodetectors have been reported using 2D and 1D chiral perovskites [16, 127], their degree of chirality typically ranging from $g_{abs} \sim 10^{-3}-10^{-1}$, which restricts their application for sensitive CPL detection. However a 1D chiral perovskite based on NEA as spacer, (*R*-, *S*-NEA)PbI_3, reported by Ishii *et al* which is grown perpendicularly to the substrate, to promote charge carrier transport to the electrode, has shown an impressive anisotropy factor of 1.85 whilst maintaining efficient charge transport. This is promising for the use of chiral perovskites in CPL photodetectors.

In addition to CPL absorption, spin-dependent, circularly polarized photoluminescence (PL) has also been realized in chiral perovskites. Long *et al* showed that in a pure (*R*-, *S*-MBA)2PbBr4 2D perovskite no PL is observed whereas for the quasi-2D *n* = 2 RD perovskite a 3% spin-polarized PL is observed [165]. This is

Figure 15. Schematic illustration of chiral RD perovskites with different number of inorganic layers (*n*). Chirality decreases with increasing layer number (*n*), and strong photoluminescence (PL) can be obtained through efficient energy funneling to the higher *n* component. Reproduced from [165], with permission from Springer Nature.

done by exploiting the *n*-phases distribution that is established when this quasi-2D perovskite is synthesized, and observing that low *n*-phases show strong chirality and high *n*-phases show strong CPL PL as shown in figure 15.

Hence, there is potential in chiral perovskites as CPL photodetectors and emitters, but their properties can be improved by using them in heterostructures. Chiral heterostructures have shown to result in a similar, or even higher degree of chirality with respect to chiral perovskites [181, 182]. However, depending on the application at hand, one needs to consider whether one grows a 3D perovskite first, and then grow a chiral perovskite on the surface, or grow a chiral perovskite first, and a 3D perovskite on top of this. For example, when a spin-LED is desired as application, one grows a chiral perovskite shell to work as spin-filter and a 3D perovskite nanocrystal as core to have the spin-polarized property without sacrificing the core's structure symmetry and luminescence property [183]. However, when one wants a device to detect CPL, a 2D perovskite needs to be grown on a 3D perovskite nanocrystal. A heterostructure CPL detector of this form was built consisting of $MAPbI_3$ and $(R\text{-}BPEA)_2PbI_4$ ($R\text{-}BPEA = R\text{-}1\text{-}(4\text{-}bromophenyl)ethylammonium$) by Zhang *et al* and the reason for this is that upon CPL excitation, the incident photons are absorbed by $MAPbI_3$, which spin-selectively transports charge to the chiral $(R\text{-}BPEA)_2PbI_4$, generating a CPL-dependent photoresponse [182].

Another unique property of chiral perovskites is the chiral induced spin selectivity (CISS) effect, which can directly control and generate spin polarization in the material based on the handedness of the chiral ligands. It is unknown how exactly the spin-filtering, or the CISS-mechanism, occurs in chiral perovskites. Nonetheless, spin polarization in chiral perovskites is high and can reach values close to 100% at room temperature [142, 184]. The CISS typically refers to the ability of chiral materials to act as spin filters for electron transport. However, a recent review by Bloom *et al* discusses that charge flow is not necessary; displacement currents arising from charge polarization can also lead to spin polarization [185]. In the realm of spin-filtering for 2D chiral perovskites, Jana *et al* have established a generic local structural descriptor ($\Delta\beta_{in}$), which signifies the local inversion asymmetry and quantitatively correlates with DFT-predicted spin-splitting in a number of 2D chiral perovskites [186]. To further enhance the functionalities of chiral perovskites, a better understanding is needed of both chirality transfer from the chiral ligands to the inorganic framework and of the exact working mechanism of CISS. An improved understanding of the intercalation mechanism of the chiral ligands will also help to design chiral perovskites with a higher anisotropy factor and thus better chiroptical properties.

Apart from these functionalities obtained with the incorporation of insulating chiral ligands with a center of chirality, there are also other ligands, which can bring novel functionalities to perovskites. For instance, a recent review by Dou *et al* discusses the incorporation of semiconductor ligands into perovskite with which one can tailor the energy landscape, carrier dynamics, and electron/ion transport properties for device applications [187]. In particular, charge transfer issues in both solar cells and LEDs can potentially be addressed by using semiconductor ligands instead of insulating ligands, but the research into this area is still in its infancy. Besides potentially fixing charge transfer issues, tailoring the band alignment between the perovskite and the semiconductor ligand can also tune the photoluminescence of the system. Presently, only type I and type II band alignments have been achieved at the organic-inorganic interface whilst a type III

alignment remains unrealized. A type III band alignment would be desirable for applications where spontaneous charge transfer or doping is needed.

In addition to the introduction of semiconductor ligands into the perovskites, also the introduction of axially chiral ligands into perovskites can offer new functionalities. As discussed in section 3, the hindered rotation of axially chiral molecules causes their chirality of which the rotational barrier is dependent on temperature, pressure and pH of the environment. Therefore, the chirality of these ligands is reversible under the influence of external stimuli such as temperature and pressure. As a result, the introduction of these ligands into perovskites can potentially be used for thermal- or pressure-based switches. A crucial aspect in these systems is the extent and maintenance of the torsional degree of the axially chiral ligands [188, 189]. The torsional angle influences the degree of non-planarity in the ligands, which can result in more pronounced chirality. In perovskite systems, the packing within the inorganic perovskite framework is critical in chirality transfer from the ligands to the inorganic perovskite framework. This transfer can be affected by the torsional degree as well as by hydrogen bonding, $\pi - \pi$ stacking, and van der Waals forces. The stability of chirality may also be affected by the torsional angle. If the angle is too small, the ligand might not maintain its chirality and undergo racemization. Control over this angle during synthesis is essential for the functionalization of perovskites using axially chiral ligands. This control can be achieved by selecting appropriate substituents to induce a certain torsional angle or by adjusting reaction conditions to favor certain conformations. In conclusion, further research is needed on how these axially chiral ligands can be incorporated and transfer their chirality to the inorganic perovskite framework.

5. Discussion

This review presents a thorough analysis of the synthesis methods for low-dimensional chiral perovskites, with a particular focus on chiral organic ligands and their impact on the structural and optoelectronic properties of chiral perovskites. We explore the complex factors that influence the growth and precise control of these chiral structures, discussing techniques such as one-step spin coating and the application of pre-synthesized single crystal powders. Additionally, the review examines the effects of substrate temperature and solvent interactions, underlining their significant roles in determining the morphology, phase distribution, and growth orientation of the perovskites. We also discuss solvent engineering and the utilization of additives, emphasizing their importance in stabilizing intermediate phases and guiding the growth process, crucial for achieving desired structural characteristics and ensuring phase purity. Finally, we provide an outlook on several promising aspects that hold potential for a deeper understanding of this fascinating class of materials and could open doors for novel devices and applications.

Enhanced control over structural chirality through further research at the molecular level is promising for materials with highly specific optoelectronic properties. This could include exploring new chiral ligands or modifying existing ones, such as by adjusting their dimensionality, to refine control over perovskite chirality. The dimensionality of chiral perovskites significantly influences their charge/spin transport and optical properties. For example, 1D chiral perovskites have greater optical responses but lower charge mobility compared to 2D ones. Other structures, like quasi-2D and 3D perovskites, and nanocrystals, offer a balance between charge transport efficiency and optical performance. However, creating these structures is challenging, attributed to difficulties in achieving phase purity for quasi-2D perovskites and managing surface chemistry for 3D and nanocrystal systems. Altering the composition of chiral perovskites, including different metals and organic components, is crucial for optimizing optoelectronic responses. Transition metals like Cu, Mn, and Fe can modify magnetic properties and affect spin selectivity. The use of axial chirality in devices responsive to external stimuli such as temperature and strain shows potential for developing adaptive sensors and optics. Integrating semiconductor ligands aligns the energy levels of organic and inorganic components within chiral perovskites, enhancing carrier and spin transport, and potentially addressing charge transfer issues.

Investigating the growth mechanisms of chiral perovskites is essential, covering crystallization processes and solvent interactions. The crystallization process, including nucleation and crystal growth, is fundamental. Understanding nucleation involves studying factors like solution supersaturation and the role of impurities or seed crystals in initiating crystal formation. The subsequent crystal growth phase, where temperature variations and solvent evaporation rates significantly impact crystal size, shape, and quality, is equally crucial. Additionally, solvent-perovskite interactions play a significant role in crystallization, affecting the structure and purity of the perovskites. How solvents interact with solutes and how solvent evaporation is managed can greatly influence the uniformity and quality of the perovskite crystals. Moreover, the dynamics of phase transformation in chiral perovskites are crucial for understanding their stability and manipulation. This involves studying phase transitions and how external conditions like temperature and pressure affect these transformations, to identify the most stable forms of these materials. A molecular-level understanding

is also essential, particularly in how molecular arrangements within the perovskite structure change during growth and how chirality is incorporated and maintained.

Incorporating chiral perovskites into practical devices like spintronic devices, chiroptical sensors, and photovoltaic cells, represent significant challenges. This involves material synthesis from solution and growth on substrates, and its interactions with adjacent layers in devices. The exploration of the following three aspects can accelerate their developments: surface engineering of substrates, new deposition techniques, and post-deposition treatment. Surface engineering, such as applying self-assembled monolayers on substrates, can induce specific orientations or phases of perovskite crystal growth. Advanced coating methods like chemical vapor deposition, pulsed laser deposition, or molecular beam epitaxy could offer precise control over film thickness and composition. Post-deposition thermal annealing improves the crystallinity and phase purity of perovskite films, helping in relieving strain, repairing defects, and ensuring a more uniform and stable film.

In summary, chiral perovskites, being a more recent focus in materials science, offer unique applications in areas like spintronics and chiroptical sensors, contrasting the long-standing research on solar cell perovskites aimed at energy efficiency. The study of chiral perovskites, with their complex synthesis and specialized uses, can benefit from the advances in solar cell perovskites, particularly in improving material fabrication methods. This knowledge transfer can expedite innovations in chiral perovskite research, focusing on their distinct properties and applications. By further development in the above highlighted aspects, researchers can significantly enhance control over the growth of chiral perovskites in various dimensions, compositions, and on substrates in devices, improving performance and reliability in practical applications. This control is vital for integrating chiral perovskites into sophisticated optoelectronic devices, where the precision of the material layer and interface quality directly impacts device efficiency and longevity.

Data availability statement

No new data were created or analysed in this study.

Acknowledgments

ORCID iDs

Sander Driessen ⦿ https://orcid.org/0009-0005-8573-8673
Sevgi Sarigul-Ozbek ⦿ https://orcid.org/0000-0002-0676-2415
Carolin M Sutter-Fella ⦿ https://orcid.org/0000-0002-7769-0869
Shuxia Tao ⦿ https://orcid.org/0000-0002-3658-8497

References

[1] Dong R, Fang Y, Chae J, Dai J, Xiao Z, Dong Q, Yuan Y, Centrone A, Zeng X C and Huang J 2015 *Adv. Mater.* **27** 1912–8
[2] Chen Y, Yi H T, Wu X, Haroldson R, Gartstein Y N, Rodionov Y I, Tikhonov K S, Zakhidov A, Zhu X Y and Podzorov V 2016 *Nat. Commun.* **7** 12253
[3] Ke L, Luo S, Ren X and Yuan Y 2021 *J. Appl. Phys.* **54** 163001
[4] Saparov B and Mitzi D B 2016 *Chem. Rev.* **116** 4558–96
[5] Son J *et al* 2023 *Nat. Commun.* **14** 3124
[6] Kelvin L 1894 *Molecular Tactics of a Crystal* (Clarendon)
[7] Gal J 2017 *Nat. Chem.* **9** 604–5
[8] Ma W, Xu L, De Moura A F, Wu X, Kuang H, Xu C and Kotov N A 2017 *Chem. Rev.* **117** 8041–93
[9] Billing D G and Lemmerer A 2003 *Acta Crystall.* E **59** m381–3
[10] Billing D G and Lemmerer A 2006 *CrystEngComm* **8** 686–95
[11] Ahn J, Lee E, Tan J, Yang W, Kim B and Moon J 2017 *Mater. Horiz.* **4** 851–6
[12] Long G, Zhou Y, Zhang M, Sabatini R, Rasmita A, Huang L, Lakhwani G and Gao W 2019 *Adv. Mater.* **31** 07628
[13] Ju T Y, Fan C C, Liang B D, Liu C D, Jin M L, Chai C Y and Zhang W 2024 *Adv. Funct. Mater.* **34** 2316747
[14] Wang J, Lu H, Pan X, Xu J, Liu H, Liu X, Khanal D R, Toney M F, Beard M C and Vardeny Z V 2021 *ACS Nano* **15** 588–95
[15] Lu H, Wang J, Xiao C, Pan X, Chen X, Brunecky R, Berry J J, Zhu K, Beard M C and Valy Vardeny Z 2019 *Sci. Adv.* **5** eaay0571
[16] Kim Y H *et al* 2021 *Science* **371** 2023
[17] Chen C, Gao L, Gao W, Ge C, Du X, Li Z, Yang Y, Niu G and Tang J 2019 *Nat. Commun.* **10** 1927
[18] Zheng Y, Xu J and Bu X H 2022 *Adv. Opt. Mater.* **10** 2101545

[19] Jana M K, Song R, Liu H, Khanal D R, Janke S M, Zhao R, Liu C, Valy Vardeny Z, Blum V and Mitzi D B 2020 *Nat. Commun.* **11** 4699
[20] Pols M, Brocks G, Calero S and Tao S 2024 Temperature-dependent chirality in halide perovskites *J. Phys. Chem. Lett.* **15** 8057–64
[21] Ma S, Ahn J and Moon J 2021 *Adv. Mater.* **33** 2005760
[22] Lu H, Vardeny Z V and Beard M C 2022 *Nat. Rev. Chem.* **6** 470–85
[23] Xu J, Li X, Xiong J, Yuan C, Semin S, Rasing T and Bu X H 2020 *Adv. Mater.* **32** 1806736
[24] Long G, Sabatini R, Saidaminov M I, Lakhwani G, Rasmita A, Liu X, Sargent E H and Gao W 2020 *Nat. Rev. Mater.* **5** 423–39
[25] Dong Y, Zhang Y, Li X, Feng Y, Zhang H and Xu J 2019 *Small* **15** 1902237
[26] Dang Y, Liu Y, Sun Y, Yuan D, Liu X, Lu W, Liu G, Xia H and Tao X 2015 *CrystEngComm* **17** 665–70
[27] Gao Q, Qi J, Chen K, Xia M, Hu Y, Mei A and Han H 2022 *Adv. Mater.* **34** 2200720
[28] Yang S, Jang G, Lee C U, Son J, Lee J, Jeong W, Roe D G, Cho J H and Moon J 2024 *Adv. Funct. Mater.* **34** 2310917
[29] Ma J, Wang H and Li D 2021 *Adv. Mater.* **33** 2008785
[30] Wang J, Fang C, Ma J, Wang S, Jin L, Li W and Li D 2019 *ACS Nano* **13** 9473–81
[31] Dunlap-Shohl W A, Zhou Y, Padture N P and Mitzi D B 2019 *Chem. Rev.* **119** 3193–295
[32] Wang S *et al* 2022 *Mater. Horiz.* **9** 2633–43
[33] Liao K, Li C, Xie L, Yuan Y, Wang S, Cao Z, Ding L and Hao F 2020 *Nano-Micro Lett.* **12** 156
[34] Xue C, Shi Y, Zhang C, Lv Y, Feng Y, Tian W, Jin S and Ma T 2019 *J. Power Sources* **422** 156–62
[35] Dai Q, Ling Q, Huang L, Liu X, Zhang H, Zhang J, Zhu Y and Hu Z 2023 *ACS Appl. Energy Mater.* **6** 1585–94
[36] Chen A Z, Shiu M, Ma J H, Alpert M R, Zhang D, Foley B J, Smilgies D M, Lee S H and Choi J J 2018 *Nat. Commun.* **9** 1336
[37] Sidhik S *et al* 2021 *Adv. Mater.* **33** 2007176
[38] Stoumpos C C, Cao D H, Clark D J, Young J, Rondinelli J M, Jang J I, Hupp J T and Kanatzidis M G 2016 *Chem. Mater.* **28** 2852–67
[39] Li S *et al* 2024 *Nat. Commun.* **15** 2573
[40] Hoffman J M, Strzalka J, Flanders N C, Hadar I, Cuthriell S A, Zhang Q, Schaller R D, Dichtel W R, Chen L X and Kanatzidis M G 2020 *Adv. Mater.* **32** 2002812
[41] Porter D A, Easterling K E and Sherif M Y 2021 *Phase Transformations in Metals and Alloys* 4th edn
[42] Chen K, Schünemann S, Song S and Tüysüz H 2018 *Chem. Soc. Rev.* **47** 7045–77
[43] Lehner L E *et al* 2023 *Adv. Mater.* **35** 2208061
[44] Zhumekenov A A *et al* 2017 *ACS Energy Lett.* **2** 1782–8
[45] Chen A Z, Shiu M, Deng X, Mahmoud M, Zhang D, Foley B J, Lee S-H, Giri G and Choi J J 2019 *Chem. Mater.* **31** 1336–43
[46] Liu N, Liu P, Ren H, Xie H, Zhou N, Gao Y, Li Y, Zhou H, Bai Y and Chen Q 2020 *ACS Appl. Mater. Interfaces* **12** 3127–33
[47] Li B *et al* 2023 *Adv. Funct. Mater.* **33** 2300216
[48] Liu L *et al* 2020 *Angw. Chem. - Int. Edn* **59** 5979–87
[49] Quintero-Bermudez R, Gold-Parker A, Proppe A H, Munir R, Yang Z, Kelley S O, Amassian A, Toney M F and Sargent E H 2018 *Nat. Mater.* **17** 900–7
[50] Xu Y, Wang M, Lei Y, Ci Z and Jin Z 2020 *Adv. Energy Mater.* **10** 2002558
[51] Li F, Zhang J, Jo S B, Qin M, Li Z, Liu T, Lu X, Zhu Z and Jen A K 2020 *Small Methods* **4** 1900831
[52] Myae Soe C M *et al* 2019 *Proc. Natl Acad. Sci. USA* **116** 58–66
[53] Qin Z, Pols M, Qin M, Zhang J, Yan H, Tao S and Lu X 2023 *ACS Energy Lett.* **8** 3188–95
[54] Wang Z, Wei Q, Liu X, Liu L, Tang X, Guo J, Ren S, Xing G, Zhao D and Zheng Y 2021 *Adv. Funct. Mater.* **31** 2008404
[55] Hoffman J M *et al* 2019 *J. Am. Chem. Soc.* **141** 10661–76
[56] Yuan Z *et al* 2017 *Nat. Commun.* **8** 14051
[57] Mao L, Guo P, Kepenekian M, Hadar I, Katan C, Even J, Schaller R D, Stoumpos C C and Kanatzidis M G 2018 *J. Am. Chem. Soc.* **140** 13078–88
[58] Liu C-D, Fan C-C, Liang B-D, Chai C-Y, Jing C-Q, Han X-B and Zhang W 2023 *ACS Mater. Lett.* **5** 1974–81
[59] Lin H *et al* 2017 *Chem. Sci.* **8** 8400–4
[60] Rahaman M Z, Ge S, Lin C-H, Cui Y and Wu T 2021 *Small Struct.* **2** 2000062
[61] Duan D, Ge C, Rahaman M Z, Lin C-H, Shi Y, Lin H, Hu H and Wu T 2023 *NPG Asia Mater.* **15** 8
[62] Ishii A and Miyasaka T 2020 *Sci. Adv.* **6** eabd3274
[63] Hu Q, Yu H, Gong S, Han Q and Wu W 2022 *J. Mater. Chem.* **10** 6002–8
[64] Han S, Liu X, Liu Y, Xu Z, Li Y, Hong M, Luo J and Sun Z 2019 *J. Am. Chem. Soc.* **141** 12470–4
[65] Li X, Hoffman J M and Kanatzidis M G 2021 *Chem. Rev.* **121** 2230–91
[66] Du K-Z, Tu Q, Zhang X, Han Q, Liu J, Zauscher S and Mitzi D B 2017 *Inorg. Chem.* **56** 9291–302
[67] Passarelli J V, Fairfield D J, Sather N A, Hendricks M P, Sai H, Stern C L and Stupp S I 2018 *J. Am. Chem. Soc.* **140** 7313–23
[68] Zhang X *et al* 2018 *Adv. Mater.* **30** 1707166
[69] Ji T *et al* 2022 *J. Mater. Chem. A* **10** 13625–50
[70] Hamill J C, Schwartz J and Loo Y-L 2018 *ACS Energy Lett.* **3** 92–97
[71] Romiluyi O, Eatmon Y, Ni R, Rand B P and Clancy P 2021 *J. Mater. Chem. A* **9** 13087–99
[72] Jiang J, Vicent-Luna J M and Tao S 2022 *J. Energy Chem.* **68** 393–400
[73] Li W, Fan J, Li J, Mai Y and Wang L 2015 *J. Am. Chem. Soc.* **137** 10399–405
[74] Gao L, Zhang F, Xiao C, Chen X, Larson B W, Berry J J and Zhu K 2019 *Adv. Funct. Mater.* **29** 1901652
[75] Cao D H, Stoumpos C C, Yokoyama T, Logsdon J L, Song T-B, Farha O K, Wasielewski M R, Hupp J T and Kanatzidis M G 2017 *ACS Energy Lett.* **2** 982–90
[76] Saidaminov M I, Spanopoulos I, Abed J, Ke W, Wicks J, Kanatzidis M G and Sargent E H 2020 *ACS Energy Lett.* **5** 1153–5
[77] Heo Y J *et al* 2021 *Adv. Funct. Mater.* **31** 2106974
[78] Laurence C and Gal J F 2009 *Lewis Basicity and Affinity Scales: Data and Measurement* (Wiley) pp 75–78
[79] Cataldo F 2015 *Eur. Chem. Bull.* **4** 92–97
[80] Davy M M, Jadel T M, Qin C, Luyun B and Mina G 2021 *Sustain. Energy Fuels* **5** 34–51
[81] Li T, Pan Y, Wang Z, Xia Y, Chen Y and Huang W 2017 *J. Mater. Chem. A* **5** 12602–52
[82] Wang J *et al* 2020 *Solar RRL* **4** 2070124
[83] Wang J *et al* 2020 *Nat. Commun.* **11** 582
[84] Jiao J, Yang C, Wang Z, Yan C and Fang C 2023 *Res. Eng.* **18** 101158
[85] Odysseas Kosmatos K, Theofylaktos L, Giannakaki E, Deligiannis D, Konstantakou M and Stergiopoulos T 2019 *Energy Environ. Mater.* **2** 79–92

[86] Tang G, Yang C, Stroppa A, Fang D and Hong J 2017 *J. Chem. Phys.* **146** 224702
[87] Xu C, Cheng L, Li Z, Zheng X, Shan S, Chen T, Fu W, Yang Y, Zuo L and Chen H 2023 *Adv. Energy Mater.* **13** 2300168
[88] Fu W, Wang J, Zuo L, Gao K, Liu F, Ginger D S and Jen A K 2018 *ACS Energy Lett.* **3** 2086–93
[89] Zou S *et al* 2023 *ACS Appl. Mater. Interfaces* **15** 26778–86
[90] Yan X, Hu S, Zhang Y, Li H and Sheng C 2019 *Sol. Energy Mater. Sol. Cells* **191** 283–9
[91] Liang C *et al* 2021 *Nat. Energy* **6** 38–45
[92] Ru Y, Zhang B, Yong X, Sui L, Yu J, Song H and Lu S 2023 *Adv. Mater.* **35** 2207265
[93] Cui Y, Jiang J, Mi W and Xiao Y 2023 *Cell Rep. Phys. Sci.* **4** 101299
[94] Zhao Y, Li X, Feng J, Zhao J, Guo Y, Yuan M, Chen G, Gao H, Jiang L and Wu Y 2022 *Giant* **9** 100086
[95] Peng X L, Han R R, Tang Y Z, Tan Y H, Fan X W, Wang F X and Zhang H 2023 *Chemistry* **18** e202201206
[96] Peng Y, Wang X, Li L, Ye H, Yang S, Yang H G, Luo J and Hou Y 2023 *Adv. Opt. Mater.* **11** 2201888
[97] Chai C-Y *et al* 2023 *Adv. Opt. Mater.* **11** 2201996
[98] Cao Q, Song R, Chan C C S, Wang Z, Wong P Y, Wong K S, Blum V and Lu H 2023 *Adv. Opt. Mater.* **11** 2203125
[99] Zhu Z K, Zhu T, Wu J, You S, Yu P, Liu X, Li L, Ji C and Luo J 2023 *Adv. Funct. Mater.* **33** 2214660
[100] Gao W *et al* 2022 *J. Energy Chem.* **68** 789–96
[101] Su W and Yuan F 2022 *Sci. Bull.* **67** 1535–8
[102] Uthoff F, Sato H and Gröger H 2017 *ChemCatChem* **9** 555–8
[103] Dai L, Chen Y Y, Xiao L J and Zhou Q L 2023 *Angw. Chem., Int. Edn* **62** e202304427
[104] Rouf A and Taneja S C 2014 *Chirality* **26** 63–78
[105] Gustafson K P, Görbe T, de Gonzalo-Calvo G, Yuan N, Schreiber C L, Shchukarev A, Tai C W, Persson I, Zou X and Bäckvall J E 2019 *Chem. Eur. J.* **25** 9174–9
[106] Paetzold J and Bäckvall J E 2005 *J. Am. Chem. Soc.* **127** 17620–1
[107] Hoben C E, Kanupp L and Bäckvall J E 2008 *Tetrahedron Lett.* **49** 977–9
[108] Jeon H, Yoon S, Ahsan M M, Sung S, Kim G-H, Sundaramoorthy U, Rhee S-K and Yun H 2017 *Catalysts* **7** 251
[109] Tseliou V, Knaus T, Vilím J, Masman M F and Mutti F G 2020 *ChemCatChem* **12** 2184–8
[110] Patil M D, Yoon S, Jeon H, Khobragade T P, Sarak S, Pagar A D, Won Y and Yun H 2019 *Catalysts* **9** 600–13
[111] Huang X, Ortiz-Marciales M, Huang K, Stepanenko V, Merced F G, Ayala A M, Correa W and De Jesús M 2007 *Org. Lett.* **9** 1793–5
[112] Allwein S P, McWilliams J C, Secord E A, Mowrey D R, Nelson T D and Kress M H 2006 *Tetrahedron Lett.* **47** 6409–12
[113] Reid J P and Goodman J M 2017 *Org. Biomol. Chem.* **15** 6943–7
[114] Prieto L, Reyes E, Uria U, Carrillo L and Vicario J L 2023 *Asian J. Org. Chem.* **12** e202300163
[115] Braire J, Macé A, Zaier R, Cordier M, Vidal J, Lalli C, Martel A and Carreaux F 2023 *J. Org. Chem.* **88** 1469–92
[116] Liu H, Gong Z-R, Zhao Y, Zheng J, Xu Y-J and Dong L 2023 *J. Org. Chem.* **88** 6108–19
[117] Urbano A, Vallejo S, Cabrera-Afonso M J and Yonte E 2020 *Org. Lett.* **22** 6122–6
[118] Chen S, Ge Z, Jia Q, Wang K-P, Gan L-H and Hu Z-Q 2019 *Chemistry* **14** 1462–6
[119] Sarigul S and Dogan I 2016 *J. Org. Chem.* **81** 5895–902
[120] Erol S and Dogan I 2013 *Tetrahedron* **69** 1337–44
[121] Erol S and Dogan I 2007 *J. Org. Chem.* **72** 2494–500
[122] Tuncel S T, Gunal S E, Ekizoglu M, Gokhan Kelekci N, Erdem S S, Bulak E, Frey W and Dogan I 2019 *J. Mol. Struct.* **1179** 40–56
[123] Jiang Z, Gao T, Liu H, Shaibani M S and Liu Z 2020 *Dyes Pigm.* **175** 108168
[124] Takaishi K, Iwachido K and Ema T 2020 *J. Am. Chem. Soc.* **142** 1774–9
[125] Feng H, Pu J, Wang S, Jiang S, Yang W, Cao D and Feng Y-S 2023 *Dyes Pigm.* **217** 111422
[126] Takaishi K, Hinoide S, Matsumoto T and Ema T 2019 *J. Am. Chem. Soc.* **141** 11852–7
[127] Zheng A, Xie X, Wang Y, Xu N, Zhang J, Yuan Y and Wang P 2021 *Adv. Funct. Mater.* **31** 2009854
[128] Sohncke L 1879 *Entwickelung Einer Theorie der Krystallstruktur* (B.G. Teubner)
[129] Richardson F S and Riehl J P 1977 *Chem. Rev.* **77** 773–92
[130] Riehl J P and Richardson F S 1986 *Chem. Rev.* **86** 1–16
[131] Hu S, Tang B, Kershaw S V and Rogach A L 2023 *ACS Appl. Mater. Interfaces* **15** 27307–15
[132] Ma J, Fang C, Chen C, Jin L, Wang J, Wang S, Tang J and Li D 2019 *ACS Nano* **13** 3659–65
[133] Pan R, Hu J, Tao S, Kan L, Yu H and Wang K 2022 *J. Mater. Chem.* **113** 16706–13
[134] Scalon L *et al* 2023 *Adv. Opt. Mater.* **12** 2300776
[135] Zhu H *et al* 2022 *ACS Appl. Mater. Interfaces* **15** 9978–86
[136] Chun J Y, Kim B G, Jang W and Wang D H 2022 *Appl. Surf. Sci.* **591** 153207
[137] Dang Y, Liu X, Sun Y, Song J, Hu W and Tao X 2020 *J. Phys. Chem. Lett.* **11** 1689–96
[138] Zhao L, Han X, Zheng Y, Yu M-H and Xu J 2021 *Adv. Photon. Res.* **2** 2100056
[139] Wang S, Guloy A, Mitzi D B and Feild C A 1995 *J. Am. Chem. Soc.* **117** 5297–302
[140] Fabini D H, Seshadri R and Kanatzidis M G 2020 *MRS Bull.* **45** 467–77
[141] Tao K, Li Q and Yan Q 2024 *Adv. Opt. Mater.* **12** 2400018
[142] Lu H *et al* 2020 *J. Am. Chem. Soc.* **142** 13030–40
[143] Fortino M, Mattoni A and Pietropaolo A 2023 *J. Mater. Chem.* **11** 9135–43
[144] Li X, Guan Y, Li X and Fu Y 2022 *J. Am. Chem. Soc.* **144** 18030–42
[145] Mihalyi-Koch W *et al* 2023 *J. Am. Chem. Soc.* **145** 28111–23
[146] Zhang M, Zhang B, Yang D and Wang Y 2021 *Inorg. Chem.* **60** 18483–9
[147] Yao L, Xue K-H, Tong H, Chen C, Niu G, Yang W and Tang J 2022 *Cryst. Growth Des.* **22** 5552–8
[148] Han X *et al* 2024 *Chem. Sci.* **15** 3530–8
[149] Chen D, Song Z, Yang C, Wei Y, Liu G, Meng L, Wu Q and Dang Y 2024 *Inorg. Chem.* **63** 10304–11
[150] Maughan A E, Koknat G, Sercel P C, Jana M K, Brunecky R, Mitzi D B, Berry J J, Blum V and Beard M C 2023 *Chem. Mater.* **35** 9086–101
[151] Wang M, Wang X, Zhang B, Li F, Meng H, Liu S and Zhao Q 2023 *J. Mater. Chem.* **11** 3206–12
[152] Xue J, Wang Z, Comstock A, Wang Z, Sung H H, Williams I D, Sun D, Liu J and Lu H 2022 *Chem. Mater.* **34** 2813–23
[153] Ge F, Li B H, Cheng P, Li G, Ren Z, Xu J and Bu X H 2022 *Angew. Chem., Int. Edn.* **61** e202115024
[154] Song Z, Yu B, Liu G, Meng L and Dang Y 2022 *J. Phys. Chem. Lett.* **13** 2567–75
[155] Sun B, Liu X F, Li X Y, Zhang Y, Shao X, Yang D and Zhang H L 2020 *Chem. Mater.* **32** 8914–20
[156] Li B, Yu Y, Xin M, Xu J, Zhao T, Kang H, Xing G, Zhao P, Zhang T and Jiang S 2022 *Nanoscale* **15** 1595–601

[157] Hao J, Lu H, Mao L, Chen X, Beard M C and Blackburn J L 2021 *ACS Nano* **15** 7608–17

[158] Dibenedetto A, Coccia C, Boiocchi M, Moroni M, Milanese C and Malavasi L 2024 *J. Phys. Chem. C* **128** 4803–8

[159] Wang Q, Lu Y, He R L, Chen R, Qiao L, Pan F, Yang Z and Song C 2022 *Small Methods* **6** 2201048

[160] Yao B, Wei Q, Yang Y, Zhou W, Jiang X, Wang H, Ma M, Yu D, Yang Y and Ning Z 2023 *Nano Lett.* **23** 1938–45

[161] Heindl M W *et al* 2022 *Adv. Opt. Mater.* **10** 2200204

[162] Zheng Y, Han X, Cheng P, Jia X, Xu J and Bu X H 2022 *J. Am. Chem. Soc.* **144** 16471–9

[163] Guan J, Zheng Y, Cheng P, Han W, Han X, Wang P, Xin M, Shi R, Xu J and Bu X H 2023 *J. Am. Chem. Soc.* **145** 26833–42

[164] Ma S, Jung Y K, Ahn J, Kyhm J, Tan J, Lee H, Jang G, Lee C U, Walsh A and Moon J 2022 *Nat. Commun.* **13** 3259

[165] Long G *et al* 2018 *Nat. Photon.* **12** 528–33

[166] Shpatz Dayan A, Wierzbowska M and Etgar L 2022 *Small Struct.* **3** 2200051

[167] Chen G *et al* 2023 *Nat. Chem.* **15** 1581–90

[168] Fiuza-Maneiro N, Sun K, López-Fernández I, Gómez-Graña S, Müller-Buschbaum P and Polavarapu L 2023 *ACS Energy Lett.* **8** 1152–91

[169] Kim Y H *et al* 2022 *Adv. Funct. Mater.* **32** 2200454

[170] Georgieva Z N, Bloom B P, Ghosh S and Waldeck D H 2018 *Adv. Mater.* **30** 1800097

[171] Shi Y, Duan P, Huo S, Li Y and Liu M 2018 *Adv. Mater.* **30** 1705011

[172] He T, Li J, Li X, Ren C, Luo Y, Zhao F, Chen R, Lin X and Zhang J 2017 *Appl. Phys. Lett.* **111** 151102

[173] Chen W, Zhang S, Zhou M, Zhao T, Qin X, Liu X, Liu M and Duan P 2019 *J. Phys. Chem. Lett.* **10** 3290–5

[174] Georgieva Z N, Zhang Z, Zhang P, Bloom B P, Beratan D N and Waldeck D H 2022 *J. Phys. Chem. C* **126** 15986–95

[175] Ren H, Wu Y, Wang C and Yan Y 2021 *J. Phys. Chem. Lett.* **12** 2676–81

[176] Kim Y-H *et al* 2020 *ACS Nano* **14** 8816–25

[177] Hubley A, Bensalah-Ledoux A, Baguenard B, Guy S, Abécassis B and Mahler B 2022 *Adv. Opt. Mater.* **10** 2200394

[178] Cheng X, Han Y and Cui B B 2022 *Adv. Opt. Mater.* **10** 2102224

[179] Huang Y, Luo H, Zhang B, Su K, Chen W, Sui G, Liang L, Zhang B, Song J and Gao P 2022 *Appl. Mater. Today* **28** 101550

[180] Brunetti B, Cavallo C, Ciccioli A, Gigli G and Latini A 2016 *Sci. Rep.* **6** 31896

[181] Zhang X, Liu X, Li L, Ji C, Yao Y and Luo J 2021 *ACS Cent. Sci.* **7** 1261–8

[182] Zhang X, Ye H, Liang L, Niu X, Wu J and Luo J 2022 *ACS Appl. Mater. Interfaces* **14** 36781–8

[183] Ye C, Jiang J, Zou S, Mi W and Xiao Y 2022 *J. Am. Chem. Soc.* **144** 9707–14

[184] Maiti A and Pal A J 2022 *Angew. Chem., Int. Edn,* **61** e202214161

[185] Bloom B P, Paltiel Y, Naaman R and Waldeck D H 2024 *Chem. Rev.* **124** 1950–91

[186] Jana M K, Song R, Xie Y, Zhao R, Sercel P C, Blum V and Mitzi D B 2021 *Nat. Commun.* **12** 4982

[187] Sun J, Wang K, Ma K, Park J Y, Lin Z-Y, Savoie B M and Dou L 2023 *J. Am. Chem. Soc.* **145** 20694–715

[188] Pietropaolo A, Mattoni A, Pica G, Fortino M, Schifino G and Grancini G 2022 *Chem* **8** 1231–53

[189] Rodríguez R *et al* 2023 *Chem. Eur. J.* **29** e202302254